

Generation of Conservative Dynamical Systems Based on Stiffness Encoding

Tengyu Hou¹, Hanming Bai¹, Ye Ding¹ and Han Ding^{1,2}

Abstract

Dynamical systems (DSs) provide a framework for high flexibility, robustness, and control reliability and are widely used in motion planning and physical human-robot interaction. The properties of the DS directly determine the robot's specific motion patterns and the performance of the closed-loop control system. In this paper, we establish a quantitative relationship between stiffness properties and DS. We propose a stiffness encoding framework to modulate DS properties by embedding specific stiffnesses. In particular, from the perspective of the closed-loop control system's passivity, a conservative DS is learned by encoding a conservative stiffness. The generated DS has a symmetric attraction behavior and a variable stiffness profile. The proposed method is applicable to demonstration trajectories belonging to different manifolds and types (e.g., closed and self-intersecting trajectories), and the closed-loop control system is always guaranteed to be passive in different cases. For controllers tracking the general DS, the passivity of the system needs to be guaranteed by the energy tank. We further propose a generic vector field decomposition strategy based on conservative stiffness, which effectively slows down the decay rate of energy in the energy tank and improves the stability margin of the control system. Finally, a series of simulations in various scenarios and experiments on planar and curved motion tasks demonstrate the validity of our theory and methodology.

Keywords

Dynamical system, stiffness encoding, conservativeness, passivity-based control, learning from demonstration

1 Introduction

Using dynamical systems (DSs) for robot motion planning and control problems has become popular in robotics because they can generate highly flexible and robust motion and control strategies. DS has been used in a wide variety of scenarios, ranging from performing point-to-point and periodic motions (Yao et al. 2021), such as pick-and-place and imitating specific motion patterns, to handling tasks in dynamic scenarios, such as real-time obstacle avoidance (Koptev et al. 2024), catching flying objects (Kim et al. 2014; Salehian et al. 2016), and in-hand manipulation (Khdivar and Billard 2023). DS was successfully applied to contact tasks such as assembly and polishing by properly regulating the interaction forces between the robot and the environment (Amanhoud et al. 2019, 2020).

In DS-based motion planning, for a robotic system defined in a state space $\xi \in \mathbb{R}^n$, we specify the system's motion evolution given by a suitably designed ordinary differential equation $\dot{\xi} = f(\xi)$, where $f(\xi) \in \mathbb{R}^n$ is a continuously differentiable vector field.

1.1 Learning DS from demonstrations

Learning from Demonstration (LfD) is a powerful method for effectively imitating task patterns by observing demonstration tasks. Many learning methods have been developed to generate DSs with stability guarantees, ensuring stability at the kinematic level.

A natural idea is to obtain stability constraints from Lyapunov's second method. Khansari-Zadeh and Billard

(2011) seminally introduced the stable estimator of dynamical systems (SEDS). They introduced constraints in the Gaussian Mixture Regression (GMR) framework based on the quadratic Lyapunov function (QLF), thus ensuring that the generated motion is globally asymptotically stable (GAS). Although using QLF simplifies the parameter estimation process for DS, SEDS can only accurately inscribe motion trajectories with a monotonically decreasing L_2 -norm distance from the equilibrium point. To overcome this problem, Figueroa and Billard (2018) entirely use the properties of a polytopic linear parameter varying (LPV) system. They propose the DS learning method LPV-DS in combination with parametrized QLF (P-QLF), which exhibits excellent reproduction accuracy for general nonlinear motions. Mohammad Khansari-Zadeh and Billard (2014) further proposed the weighted sum of asymmetric quadratic functions (WSAQF), which achieves a wider range of fitting capabilities while satisfying global validity. Combined with WSAQF, the control corrections are obtained

¹State Key Laboratory of Mechanical System and Vibration, School of Mechanical Engineering, Shanghai Jiao Tong University, Shanghai 200240, China

²State Key Laboratory of Intelligent Manufacturing Equipment and Technology, School of Mechanical Science and Engineering, Huazhong University of Science and Technology, Wuhan, Hubei 430074, China

Corresponding author:

Ye Ding, State Key Laboratory of Mechanical System and Vibration, School of Mechanical Engineering, Shanghai Jiao Tong University, Shanghai 200240, China.

Email: y.ding@sjtu.edu.cn

by solving the convex optimization problem with constraints in real time, thus ensuring that the system is GAS. [Kronander et al. \(2015\)](#) proposed locally modulated DS (LMDS) based on Lyapunov theory. This method locally shapes the existing DS through a modulation matrix while ensuring that the modulated DS is locally asymptotically stable (LAS). To address the problem of robots failing to track a specific reference trajectory when perturbed, [Figueroa and Billard \(2022\)](#) novelly proposed locally active globally stable DS (LAGS-DS), which causes the DS to exhibit stiffness-like symmetric attraction behaviors.

To ensure stability at the kinematic level, contraction analysis and partial contraction analysis are also effective tools to provide stability constraints ([Lohmiller and Slotine 1998](#); [Wang and Slotine 2005](#)). The contraction theory ensures that all DS trajectories converge exponentially to each other and that the trajectories globally exponentially converge towards the equilibrium point. Similar to the real-time correction strategy in [Mohammad Khansari-Zadeh and Billard \(2014\)](#), [Blocher et al. \(2017\)](#) computed the control inputs based on the contraction theory to online stabilize the original DS with the spurious attractor. [Ravichandar et al. \(2017\)](#) generated nonlinear trajectories with guaranteed exponential convergence conditions by providing stability constraints through partial contraction analysis. Further, [Ravichandar and Dani \(2019\)](#) learned position and orientation dynamics based on contraction theory.

A framework for learning diffeomorphism is proposed to generate more complex trajectories while ensuring stability. Diffeomorphism establishes a one-to-one correspondence between the original space and the transformed space, thus transforming the highly nonlinear and complex learning tasks in the original space into easy-to-learn tasks in the transformed space. Since the diffeomorphism maintains the consistency of DS stability in the original and transformed spaces, the stable and highly nonlinear DS in the original space can be obtained by learning the stable DS in the transformed space. [Neumann and Steil \(2015\)](#) gave an analytic expression for diffeomorphism, which corresponds the complex Lyapunov function in the original space to the QLF in the transformed space, thus combining SEDS to generate a stable DS in the transformed space. [Perrin and Schlehuber-Caissier \(2016\)](#) use diffeomorphism to correspond complex demonstration trajectories in the original space to simple linear trajectories in the transformed space, where the diffeomorphism is the composition of the locally weighted translations.

Scholars have proposed a series of novel works using neural networks, a powerful framework, in combination with the aforementioned Lyapunov theory, contraction theory, and diffeomorphic transformation approach ([Dawson et al. 2023](#)). [Lemme et al. \(2014\)](#) learn DS vector fields based on an extreme learning machine, and Lyapunov theory guarantees DS stability. [Rana et al. \(2020\)](#) construct diffeomorphism using the non-volume preserving (NVP) network architecture, which is a general class of mappings, and its parameter optimization is achieved through back-propagation. In the deep neural network framework, [Pérez-Dattari and Kober \(2023\)](#) used imitation and contrastive learning to give a learning loss that ensures

stability, generating first-order and second-order stable DSs. Combining with the contraction theory, [Mohammadi et al. \(2024\)](#) proposed a neural network-based method to generate the contractive DS. The DS with contractive property is obtained by integrating the negative definite Jacobi matrix generated by a neural network. They further used the variational autoencoder to generate the contractive DS in high dimensional space. In addition, many scholars have used differential geometry, a powerful geometric tool, to generate DSs on manifolds ([Duan et al. 2024](#); [Fichera and Billard 2023](#)).

1.2 Research on impedance control

The aforementioned DS theory provides a powerful framework for robot trajectory planning. In realistic scenarios, considering the interaction between the robot and the environment in order for the robot to perform its tasks better, in addition to planning the robot's position and velocity, it is also necessary to compliantly regulate the interaction forces between the robot and the environment. Impedance control provides a solution to coordinate the dynamic relationship between position, velocity, and interaction forces ([Hogan 1985](#)).

When the robot interacts with the environment, an important property of the controller is passivity, which brings along advantageous robustness properties ([Ott 2008](#)). The controller's passivity allows the robot to produce stable behavior when in contact with a passive environment. In this perspective, the classical impedance controller in the regulation case is passive. When considering more complex tasks and environments, researchers often require robots to track continuous trajectories or interact with the environment exhibiting variable impedance characteristics, but these dynamic properties are achieved at the expense of impedance controller passivity. To keep the robot passive while performing tracking tasks, many scholars have advocated using a time-independent velocity field to guide the robot's motion. [Li and Horowitz \(1999\)](#) introduced the augmented coordinates to achieve the system's passivity in the framework of velocity field control (VFC) by rationally distributing the kinetic energy of the original system and the corresponding kinetic energy of the augmented coordinates. [Duindam et al. \(2004\)](#) devised a passive control rate to enable the robot to track the desired motion in an artificial potential field. Such methods are complex, and selecting the appropriate controller parameters is difficult. [Kishi et al. \(2003\)](#) ensured the system's passivity by introducing an energy tank structure to keep the direction of motion constant during trajectory tracking and regulating the velocity magnitude in real time, which degraded the tracking performance at the velocity level. Another area of research focuses on maintaining system passivity while the robot executes variable impedance control. [Ferraguti et al. \(2013\)](#) guarantee the passivity of the variable stiffness control process by incorporating an energy tank, but the discontinuous control law degrades the system's dynamic performance when the energy tank is depleted. [Kronander and Billard \(2016b\)](#) ensure that the impedance control is passive by imposing constraints on the impedance damping and stiffness matrices, but the method relies on external force measurements with an accurate dynamics model. In addition,

many passivity-based control methods in the impedance control framework have been successfully applied in flexible joint robots (Albu-Schäffer et al. 2007; Ott et al. 2008; Keppeler et al. 2018; Spyraikos-Papastavridis et al. 2020).

Combining the idea of impedance control in the DS framework, Kronander and Billard (2016a) give the widely used passive-DS controller based on the damping control law. By rational design, the impedance damping matrix can selectively dissipate energy in task-irrelevant directions, while the stiffness characteristics of the closed-loop control system are encoded in the DS $\mathbf{f}(\boldsymbol{\xi})$. It is worth noting that when the vector field $\mathbf{f}(\boldsymbol{\xi})$ is conservative, the robotic system is passive, thus ensuring stability when interacting with passive environments. The passive-DS controller ensures the system's passivity when the robot tracks a continuous trajectory and performs variable impedance control by uniformly encoding the trajectory tracking information and the variable stiffness characteristics in the DS $\mathbf{f}(\boldsymbol{\xi})$. For a general non-conservative DS, Kronander and Billard (2016a) introduced an energy tank to offset the loss of passivity due to the non-conservative component $\mathbf{f}_{nc}(\boldsymbol{\xi})$. However, when the energy in the tank is depleted, the closed-loop system's dynamic performance and trajectory tracking performance are greatly reduced due to the switching control law introduced by the energy tank structure. Therefore, solving the problem of rationally decomposing the general DS into conservative and non-conservative components to slow down the energy tank's consumption rate remains a challenge. Under the framework of the passive-DS controller, Huber et al. (2024) further design the impedance damping matrix reasonably for obstacle avoidance scenarios, effectively reducing the probability of collision. Using the optimal control technique, Fichera and Billard (2023) give a torque-based control framework for the second-order DS.

1.3 Contribution

From the above literature review, it is clear that most of the existing studies related to learning DS only consider stability at the kinematic level and do not consider the passivity of the control system (which corresponds to the conservativeness of the DS). A few studies, although learning conservative DS, are limited to the simple case of a 2D linear space and lack a systematic discussion for the generation of conservative DS on more complex trajectories or general manifolds. DS decomposition plays an important role in the performance of energy tank-based controllers. However, there is yet to be a method to propose a generic decomposition strategy. In addition, the current study only discusses the stiffness properties of DS at a qualitative level, and a systematic discussion of the stiffness properties for DS modulation is still needed.

This paper proposes a DS generation framework based on stiffness encoding, as shown in Figure 1. We establish and summarise the connection between the encoded stiffness properties and the generated DS, and generate DS to meet the requirements of specific scenarios by designing the stiffness properties. We utilize the conservative stiffness matrix to obtain conservative DS, which guarantees the passivity of the controller. We further extend our approach to generate conservative DS on different manifolds and for different trajectory types. Further, we also propose a generic

decomposition algorithm for non-conservative DS based on the conservative stiffness matrix, which significantly slows down the depletion rate of the energy tank. As shown above, we provide a systematic analysis and discussion for the conservativeness of DS.

The contribution of this paper can be summarised as follows.

1. We develop a framework for DS generation based on stiffness encoding (see Figure 1), giving the connection between stiffness properties and their corresponding DS characteristics.
2. Based on Gaussian processes, the conservative DS with a symmetric attraction behavior and a variable stiffness profile is learned in linear space. The method is further generalized to SE(3) as well as to closed-loop and self-intersecting trajectories. In all scenarios, we prove the controller's passivity.
3. Combined with the controller's energy tank structure, we propose a generic decomposition strategy for non-conservative DS based on the conservative stiffness matrix.
4. A series of simulations and experiments are conducted to validate the proposed theory and methodology.

The rest of the paper is organized as follows. Section 2 illustrates the contents of this paper in comparison with related work. Preliminaries are given in Section 3, where we introduce the framework of stiffness encoding and the necessary basics. In Section 4, we generate conservative DS with symmetric attraction properties based on Gaussian processes in a 2D linear space. A generalization of the conservative DS generation method is given in Section 5: we discuss the case on SE(3) as well as closed-loop and self-intersecting trajectories. At the same time, we propose effective DS decomposition strategies. Section 6 verifies the validity of the proposed theory and method through a series of simulations and experiments. Finally, Section 7 concludes the whole paper.

2 Related work

In our previous work, Hou et al. (2024) systematically discussed the connection between the exactness and symmetry of the stiffness matrix on the elastic force vector field it generates. The vector field is continuously distributed in space when the stiffness matrix is exact. The vector field is conservative when the stiffness matrix is exact and symmetric. In this paper, we use these quantitative relations to guide the generation of DS. In particular, on SE(3), we use the stiffness matrix's properties to generate a conservative DS (see Lemma 4). In addition to the symmetry and exactness mentioned above as properties affecting DS, negative definiteness is also important. As mentioned in Section 1.1, many works learned DS based on the contraction theory, which ensures its asymptotic stability. In this paper, we clarify that these works essentially modulate the DS at the stiffness level. The simplest case of the contraction theory is equivalent to constraining the stiffness matrix to be constantly negative definite. We first sort out and summarise the mechanisms by which exactness, symmetry, and negative definiteness affect the DS, giving a

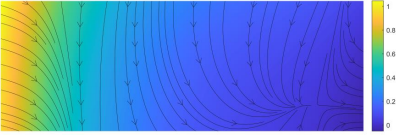

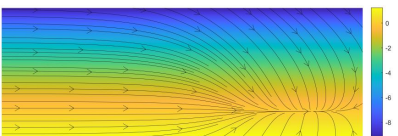
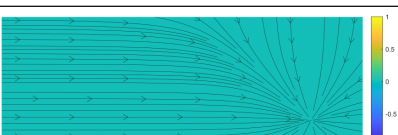
The Properties of $\mathbf{K}(\xi)$			The Schematic of DS $\mathbf{f}(\xi)$	
exact	$\frac{\partial k_{ij}}{\partial \xi^k} = \frac{\partial k_{ik}}{\partial \xi^j}$	\Rightarrow	continuous	
exact symmetric	$\frac{\partial k_{ij}}{\partial \xi^k} = \frac{\partial k_{ik}}{\partial \xi^j}$ $\mathbf{K}(\xi) = \mathbf{K}(\xi)^T$	\Rightarrow	conservative	
exact negative definite	$\frac{\partial k_{ij}}{\partial \xi^k} = \frac{\partial k_{ik}}{\partial \xi^j}$ $\mathbf{K}(\xi) + \mathbf{K}(\xi)^T \prec 0$	\Rightarrow	contractive	
exact symmetric negative definite	$\frac{\partial k_{ij}}{\partial \xi^k} = \frac{\partial k_{ik}}{\partial \xi^j}$ $\mathbf{K}(\xi) = \mathbf{K}(\xi)^T$ $\mathbf{K}(\xi) + \mathbf{K}(\xi)^T \prec 0$	\Rightarrow	conservative contractive	

Figure 1. Schematic diagram of the stiffness encoding. The color of each point in the figure indicates the value of the angular velocity of the vector field at the corresponding point. When encoding a specific stiffness, the corresponding DS exhibits particular properties. (1) When the stiffness matrix satisfies the exactness, a well-defined DS is guaranteed, i.e., a continuous vector field in space. (2) The DS is conservative when the stiffness is exact and symmetric. Conservativeness is shown in the graph as a constant angular velocity of zero. In the figure, we show a conservative DS with symmetric attraction behavior, and it is not contractive. (3) For the DS to be contractive, the encoded stiffness must satisfy both exactness and negative definiteness. It can be seen that all trajectories of the DS converge to each other. (4) The DS is conservative and contractive when the stiffness matrix is exact, symmetric, and negative definite.

framework for modulating the DS from the point of view of stiffness encoding, as shown in Figure 1. In this framework, contraction theory is naturally included, and by combining different stiffness properties, we can obtain DS of various properties.

Figueroa and Billard (2022) first clarified that stiffness-like symmetric attraction behaviors can enhance the perturbation resistance of a DS, and the robot can be quickly attracted to the demonstration trajectory after a perturbation. By designing DS with variable stiffness properties, Michel et al. (2024) enabled the robot to exhibit different impedance stiffnesses at different stages of motion, and the system was thus able to interact well with environments with different physical properties. Although the above DSs exhibit interesting stiffness properties, they are all non-conservative, and all of them require the introduction of an energy tank to ensure the passivity of the system when control is performed. Khansari-Zadeh and Khatib (2017) imitate the demonstration behavior by generating a conservative DS by learning potential functions. However, to improve the learning accuracy, they need to introduce a dissipative field, which results in the total DS no longer being conservative. In this paper, we consider the above important properties and present the generation of conservative DS with stiffness-like symmetric attraction behaviors and variable stiffness properties. We also present the generation strategy of conservative DS for more complex trajectories and spaces.

Kronander and Billard (2016a) propose a practical and effective passive-DS controller, and they further point out that non-conservativeness leads to loss of passivity, but the

decomposition of DS into conservative and non-conservative parts can alleviate this phenomenon. To address this issue, they propose vector field decomposition methods for DSs generated by specific methods (e.g., SEDS and LMDS). They use the Lyapunov function corresponding to the learning process of the DS to construct the conservative part, but this is not general, and other ways exist to improve the decomposition to a large extent. In this paper, we propose a decomposition strategy for general DS. The decomposition of DS is achieved by optimizing the decomposition index based on the energy tank structure. Simulations and experiments show that the proposed decomposition method can effectively slow down the energy decay of the energy tank.

3 Preliminaries

In this section, we give preliminaries. We begin by introducing impedance control in the DS framework, then present the idea of stiffness encoding in this paper, and finally introduce passivity analysis and Gaussian processes (GP).

3.1 Impedance Control

The rigid-body dynamics of a robotic system are described by equations based on generalized coordinates $\xi \in \mathbb{R}^n$:

$$\mathbf{M}(\xi)\ddot{\xi} + \mathbf{C}(\xi, \dot{\xi})\dot{\xi} + \mathbf{G}(\xi) = \tau_c + \tau_e, \quad (1)$$

where $\mathbf{M}(\xi) \in \mathbb{R}^{n \times n}$, $\mathbf{C}(\xi, \dot{\xi}) \in \mathbb{R}^{n \times n}$, and $\mathbf{G}(\xi) \in \mathbb{R}^n$ denote the mass matrix, the Coriolis matrix, and the gravity vector, respectively.

Based on the DS framework, [Kronander and Billard \(2016a\)](#) proposed the passive-DS controller:

$$\tau_c = \mathbf{G}(\boldsymbol{\xi}) - \mathbf{D}(\boldsymbol{\xi})(\dot{\boldsymbol{\xi}} - \mathbf{f}(\boldsymbol{\xi})) = \mathbf{G}(\boldsymbol{\xi}) - \mathbf{D}(\boldsymbol{\xi})\dot{\boldsymbol{\xi}} + \lambda_1 \mathbf{f}(\boldsymbol{\xi}). \quad (2)$$

In (2), the control damping matrix $\mathbf{D}(\boldsymbol{\xi})$ is set in the following form:

$$\mathbf{D}(\boldsymbol{\xi}) = \mathbf{Q}(\boldsymbol{\xi})\boldsymbol{\Lambda}\mathbf{Q}(\boldsymbol{\xi})^T, \quad (3)$$

where $\boldsymbol{\Lambda} = \text{diag}[\lambda_1, \dots, \lambda_n]$ ($\lambda_1, \dots, \lambda_n > 0$), and $\mathbf{Q}(\boldsymbol{\xi}) = [\mathbf{e}_1, \dots, \mathbf{e}_n]$ is the orthogonal matrix where $\mathbf{e}_1 = \mathbf{f}(\boldsymbol{\xi})/\|\mathbf{f}(\boldsymbol{\xi})\|$.

The closed loop dynamics of the robotic system (1) under controller (2) can be expressed as

$$\mathbf{M}(\boldsymbol{\xi})\ddot{\boldsymbol{\xi}} + (\mathbf{C}(\boldsymbol{\xi}, \dot{\boldsymbol{\xi}}) + \mathbf{D}(\boldsymbol{\xi}))\dot{\boldsymbol{\xi}} - \lambda_1 \mathbf{f}(\boldsymbol{\xi}) = \tau_c. \quad (4)$$

At this point, $-\lambda_1 \mathbf{f}(\boldsymbol{\xi})$ can be viewed as a nonlinear elastic force driving the robotic system. In comparison with classical impedance control, it is clear that the apparent stiffness $\mathbf{K}_a(\boldsymbol{\xi})$ of the closed-loop system (4) can be expressed as ([Chen and Kao 2000](#); [Figueroa and Billard 2022](#))

$$\mathbf{K}_a(\boldsymbol{\xi}) = \frac{\partial(-\lambda_1 \mathbf{f}(\boldsymbol{\xi}))}{\partial \boldsymbol{\xi}} = -\lambda_1 \frac{\partial \mathbf{f}(\boldsymbol{\xi})}{\partial \boldsymbol{\xi}}. \quad (5)$$

Note that λ_1 is a constant scalar in practical control, and it is clear that the first-order derivative of DS $\mathbf{f}(\boldsymbol{\xi})$ fully inscribes the stiffness properties of the closed-loop control system.

3.2 Stiffness Encoding

Section 3.1 shows that the stiffness information $\mathbf{K}(\boldsymbol{\xi}) = \frac{\partial \mathbf{f}(\boldsymbol{\xi})}{\partial \boldsymbol{\xi}}$ portrays important properties of closed-loop control systems and DS. Therefore, it is natural to think that we can obtain structure-specific DS and satisfactory system performance by carefully designing the stiffness $\mathbf{K}(\boldsymbol{\xi})$.

To design the stiffness it is first necessary to study the critical properties of the stiffness matrix. One property worth noting is the conservativeness of the stiffness matrix:

Lemma 1. Conservative stiffness matrix ([Hou et al. 2024](#)). The conservativeness of the stiffness matrix $\mathbf{K}(\boldsymbol{\xi})$ in a linear space is equivalent to the simultaneous satisfaction of symmetry and exactness:

$$\begin{cases} k_{ij} = k_{ji}, \\ \frac{\partial k_{ij}}{\partial \xi^k} = \frac{\partial k_{ik}}{\partial \xi^j}. \end{cases} \Rightarrow \begin{cases} \mathbf{f} = \oint_{\partial \Sigma} \mathbf{K}(\boldsymbol{\xi}) \cdot d\boldsymbol{\xi} = \mathbf{0}, \\ W = \oint_{\partial \Sigma} \mathbf{f} \cdot d\boldsymbol{\xi} = 0, \end{cases} \quad (6)$$

where k_{ij} means the i th row and j th column of \mathbf{K} , and $\partial \Sigma$ is an arbitrary closed path.

[Hou et al. \(2024\)](#) showed that when the stiffness matrix $\mathbf{K}(\boldsymbol{\xi})$ satisfies only exactness, the corresponding DS $\mathbf{f}(\boldsymbol{\xi}) = \oint_{\partial \Sigma} \mathbf{K}(\boldsymbol{\xi}) \cdot d\boldsymbol{\xi}$ is guaranteed to be a continuous vector field.

Contractive behavior is a property one usually expects DS to have, and the following lemma gives its definition:

Lemma 2. Contraction theory ([Lohmiller and Slotine 1998](#)). Given an autonomous DS $\dot{\boldsymbol{\xi}} = \mathbf{f}(\boldsymbol{\xi})$ and a positive definite matrix $\mathbf{U}(\boldsymbol{\xi})$, the system is said to be globally contracting with respect to $\boldsymbol{\xi}$ if it satisfies the following condition:

$$\forall \boldsymbol{\xi} \in \mathbb{R}^n, \frac{\partial \mathbf{f}(\boldsymbol{\xi})}{\partial \boldsymbol{\xi}}^T \mathbf{U}(\boldsymbol{\xi}) + \dot{\mathbf{U}}(\boldsymbol{\xi}) + \mathbf{U}(\boldsymbol{\xi}) \frac{\partial \mathbf{f}(\boldsymbol{\xi})}{\partial \boldsymbol{\xi}} \leq -\gamma_c \mathbf{U}(\boldsymbol{\xi}), \quad (7)$$

where γ_c is a positive constant. At this point, all trajectories of the above contractive system converge to each other exponentially.

In this paper, we make it clear that the contraction theory essentially constrains the DS from the stiffness level:

$$\mathbf{K}(\boldsymbol{\xi})^T \mathbf{U}(\boldsymbol{\xi}) + \dot{\mathbf{U}}(\boldsymbol{\xi}) + \mathbf{U}(\boldsymbol{\xi}) \mathbf{K}(\boldsymbol{\xi}) \leq -\gamma_c \mathbf{U}(\boldsymbol{\xi}). \quad (8)$$

When we take $\mathbf{U}(\boldsymbol{\xi}) \equiv \mathbf{I}$, contraction implies that the symmetric part of $\mathbf{K}(\boldsymbol{\xi})$ is negative definite: $\mathbf{K}(\boldsymbol{\xi}) + \mathbf{K}(\boldsymbol{\xi})^T \prec 0$.

Interestingly, we can combine the above exactness, symmetry and negative definiteness on stiffness with each other, so that we can flexibly modulate the properties of DS. The framework of stiffness encoding is shown in Figure 1.

3.3 Passivity Analysis

In scenarios where a robotic system interacts with its environment, passivity is a very important property. If the controller ensures a passive relationship between the external force and the robot velocity, then the robot will behave stably in contact with any passive environment ([Colgate and Hogan 1988](#)). The passive-DS controller (2) has the following property:

Lemma 3. ([Kronander and Billard 2016a](#)). When $\mathbf{f}(\boldsymbol{\xi})$ is conservative with the corresponding potential function $V_f(\boldsymbol{\xi})$, the system (1) controlled by (2) is passive with regard to the input-output pair $(\dot{\boldsymbol{\xi}}, \tau_c)$ with the storage function $W(\boldsymbol{\xi}, \dot{\boldsymbol{\xi}}) = \frac{1}{2} \dot{\boldsymbol{\xi}}^T \mathbf{M}(\boldsymbol{\xi}) \dot{\boldsymbol{\xi}} + \lambda_1 V_f(\boldsymbol{\xi})$.

From the stiffness point of view, combined with Lemma 3, we naturally obtain the following proposition.

Proposition 1. The system (1) is passive under joint control law $\tau_c(\boldsymbol{\xi})$ given by

$$\tau_c(\boldsymbol{\xi}) = \mathbf{G}(\boldsymbol{\xi}) - \mathbf{D}(\boldsymbol{\xi})\dot{\boldsymbol{\xi}} + \int_{\boldsymbol{\xi}_0}^{\boldsymbol{\xi}} \mathbf{K}_{ctrl}(\boldsymbol{\xi}) d\boldsymbol{\xi}, \quad (9)$$

where \mathbf{K}_{ctrl} is symmetric and exact, i.e.,

$$[\mathbf{K}_{ctrl}]_{ij} = [\mathbf{K}_{ctrl}]_{ji}, \frac{\partial [\mathbf{K}_{ctrl}]_{ki}}{\partial \xi^j} = \frac{\partial [\mathbf{K}_{ctrl}]_{kj}}{\partial \xi^i}. \quad (10)$$

The passivity of the controllers (2) and (9) imposes corresponding requirements on the property of $\mathbf{f}(\boldsymbol{\xi})$ and $\mathbf{K}(\boldsymbol{\xi})$. A conservative DS $\mathbf{f}(\boldsymbol{\xi})$ would be a better choice which would improve the performance of the controller. This paper focuses on guaranteeing the controller's passivity; hence, it concentrates on utilizing a conservative stiffness matrix to modulate the DS in the framework of stiffness encoding.

When $\mathbf{f}(\boldsymbol{\xi})$ is a non-conservative DS, one often introduces an energy tank to correct the controller ([Kronander and Billard 2016a](#)):

$$\tau_c = \mathbf{G}(\boldsymbol{\xi}) - \mathbf{D}(\boldsymbol{\xi})\dot{\boldsymbol{\xi}} + \beta(\boldsymbol{\xi}, s)\lambda_1 \mathbf{f}(\boldsymbol{\xi}), \quad (11a)$$

$$\dot{s} = \alpha(s)\dot{\boldsymbol{\xi}}^T \mathbf{D}(\boldsymbol{\xi})\dot{\boldsymbol{\xi}} - \beta(\boldsymbol{\xi}, s)\lambda_1 \dot{\boldsymbol{\xi}}^T \mathbf{f}(\boldsymbol{\xi}), \quad (11b)$$

where $\alpha(s)$ and $\beta(\boldsymbol{\xi}, s)$ are the energy tank switching functions, and $s \in [s^l, s^u]$ is the energy of the energy tank.

When the energy tank is depleted, the performance of the robotic system is affected (see Figure 11). To slow down the rate of energy depletion, the DS can be decomposed into the conservative part $\mathbf{f}_c(\boldsymbol{\xi})$ and the non-conservative part $\mathbf{f}_{nc}(\boldsymbol{\xi})$:

$$\mathbf{f}(\boldsymbol{\xi}) = \mathbf{f}_c(\boldsymbol{\xi}) + \mathbf{f}_{nc}(\boldsymbol{\xi}). \quad (12)$$

At this point the controller is shown below:

$$\boldsymbol{\tau}_c = \mathbf{G}(\boldsymbol{\xi}) - \mathbf{D}(\boldsymbol{\xi})\dot{\boldsymbol{\xi}} + \lambda_1 \mathbf{f}_c(\boldsymbol{\xi}) + \beta(\boldsymbol{\xi}, s) \lambda_1 \mathbf{f}_{nc}(\boldsymbol{\xi}), \quad (13a)$$

$$\dot{s} = \alpha(s) \dot{\boldsymbol{\xi}}^T \mathbf{D}(\boldsymbol{\xi}) \dot{\boldsymbol{\xi}} - \beta(\boldsymbol{\xi}, s) \lambda_1 \dot{\boldsymbol{\xi}}^T \mathbf{f}_{nc}(\boldsymbol{\xi}). \quad (13b)$$

As can be seen from (13), only the non-conservative part $\mathbf{f}_{nc}(\boldsymbol{\xi})$ is consuming energy. Therefore, when DS is non-conservative, a reasonable DS decomposition plays an important role in the controller performance.

3.4 Gaussian Processes

The Gaussian process (GP) used to describe the distribution of the function is completely determined by its mean function and covariance function $k^\theta(\boldsymbol{\xi}, \boldsymbol{\xi}')$, where θ is the hyperparameters of GP. In this paper, we take the mean function as zero and choose the commonly used squared exponential covariance function.

For the N training points $\mathbf{X} = [\boldsymbol{\xi}_1 \boldsymbol{\xi}_2 \cdots \boldsymbol{\xi}_N]$ and the observed target values $\mathbf{y} = [y_1 y_2 \cdots y_N]^T$, the prediction output y_{pre} corresponding to the test point $\boldsymbol{\xi}$ for GP regression can be described as

$$y_{pre} | \mathbf{X}, \mathbf{y}, \boldsymbol{\xi} \sim \mathcal{N}(\overline{y_{pre}}, \text{cov}(y_{pre})), \quad (14)$$

where

$$\begin{aligned} \overline{y_{pre}} &= gp(\boldsymbol{\theta}, \mathbf{X}, \mathbf{y}, \boldsymbol{\xi}) \\ &= K^\theta(\boldsymbol{\xi}, \mathbf{X}) [K^\theta(\mathbf{X}, \mathbf{X}) + \sigma_n^2 \mathbf{I}]^{-1} \mathbf{y}, \end{aligned} \quad (15)$$

$$\begin{aligned} \text{cov}(y_{pre}) \\ &= K^\theta(\boldsymbol{\xi}, \boldsymbol{\xi}) - K^\theta(\boldsymbol{\xi}, \mathbf{X}) [K^\theta(\mathbf{X}, \mathbf{X}) + \sigma_n^2 \mathbf{I}]^{-1} K^\theta(\mathbf{X}, \boldsymbol{\xi}). \end{aligned} \quad (16)$$

$\overline{y_{pre}}$ and $\text{cov}(y_{pre})$ are the posterior mean and covariance matrix of y_{pre} . \mathbf{I} is the $N \times N$ identity matrix. $K^\theta(\mathbf{X}, \mathbf{X})$ is the $N \times N$ covariance matrix which can be evaluated elementwise based on the training points with the covariance function $k^\theta(\boldsymbol{\xi}, \boldsymbol{\xi}')$, and similarly for $K^\theta(\boldsymbol{\xi}, \boldsymbol{\xi})$, $K^\theta(\boldsymbol{\xi}, \mathbf{X})$. σ_n^2 is the variance of the noise, contained in $\boldsymbol{\theta}$. The hyperparameters $\boldsymbol{\theta}$ can be optimized by minimizing the negative logarithmic marginal likelihood (NLML) $-\log p(\mathbf{y} | \mathbf{X}, \boldsymbol{\theta})$ (Williams and Rasmussen 2006).

4 Generation of Conservative DS

In this section, we present the conservative DS generation method with symmetric attraction property, while the stiffness is variably tunable. As can be seen from Figure 1, the DS's symmetric attraction behavior sometimes contradicts its contraction. Therefore, in this study, we focus on the symmetry and exactness of the stiffness matrix. When the stiffness \mathbf{K} is symmetric and exact, the elastic force $\mathbf{f}(\boldsymbol{\xi})$ and the corresponding potential function $V(\boldsymbol{\xi})$ can be

expressed as (see Appendix A for details)

$$\mathbf{f}(\boldsymbol{\xi}) = -\nabla V(\boldsymbol{\xi}) = \nabla g(\boldsymbol{\xi}_0) - \nabla g(\boldsymbol{\xi}), \quad (17a)$$

$$V(\boldsymbol{\xi}) = g(\boldsymbol{\xi}) - g(\boldsymbol{\xi}_0) - \nabla g(\boldsymbol{\xi}_0) \cdot (\boldsymbol{\xi} - \boldsymbol{\xi}_0), \quad (17b)$$

where $g(\boldsymbol{\xi})$ is a differentiable function that will be constructed by GP, and $\boldsymbol{\xi}_0$ is the equilibrium point of the DS.

From the previous description, $\dot{\boldsymbol{\xi}} = \mathbf{f}(\boldsymbol{\xi})$ is considered as the designed DS and $V(\boldsymbol{\xi})$ can be regarded as the Lyapunov function. According to the Lyapunov stability theory, the global asymptotic stability of the DS at point $\boldsymbol{\xi}_0$ imposes the following requirements on $V(\boldsymbol{\xi})$:

$$\begin{cases} \text{(a)} & V(\boldsymbol{\xi}) > 0 & \forall \boldsymbol{\xi} \in \mathbb{R}^n, \boldsymbol{\xi} \neq \boldsymbol{\xi}_0 \\ \text{(b)} & \dot{V}(\boldsymbol{\xi}) < 0 & \forall \boldsymbol{\xi} \in \mathbb{R}^n, \boldsymbol{\xi} \neq \boldsymbol{\xi}_0 \\ \text{(c)} & V(\boldsymbol{\xi}_0) = 0, & \dot{V}(\boldsymbol{\xi}_0) = 0. \end{cases} \quad (18)$$

It is easy to verify that condition (18) (c) is satisfied due to the form (17). Notice that $\dot{V}(\boldsymbol{\xi}) = \nabla V(\boldsymbol{\xi}) \cdot \dot{\boldsymbol{\xi}} = -\|\nabla V(\boldsymbol{\xi})\|^2$, condition (18) can be expressed as follows:

$$g(\boldsymbol{\xi}) > g(\boldsymbol{\xi}_0) + \nabla g(\boldsymbol{\xi}_0) \cdot (\boldsymbol{\xi} - \boldsymbol{\xi}_0), \boldsymbol{\xi} \neq \boldsymbol{\xi}_0 \quad (19a)$$

$$\|\nabla g(\boldsymbol{\xi}) - \nabla g(\boldsymbol{\xi}_0)\|^2 > 0, \boldsymbol{\xi} \neq \boldsymbol{\xi}_0. \quad (19b)$$

Next we will describe how to construct a suitable function $g(\boldsymbol{\xi})$ in a reasonable way, based on GP.

For the demonstration task, different demonstration trajectories differ, and our goal is for the robot to move along a trajectory that represents a common feature of the demonstration trajectories. In Section 4.1, we generate the integral path that can represent the geometrical features of the demonstration trajectories. Based on the generated integration path, the potential energy function V_p is constructed in Section 4.2. By suitable construction, the DS corresponding to V_p is conservative and has symmetric attraction behavior. However, many parameters of V_p remain to be further defined and optimized. In Section 4.3, V_p is optimized so that the actual motion velocity generated based on GP is consistent with the reference velocity $\{\boldsymbol{\xi}_i^{\text{ref}}\}_{i=1}^N$.

4.1 Generation of the Integral Path

In this section, we obtain the integral path based on the function V_1 constructed by GP.

4.1.1 Generation of the Initial Function V_0

We choose a quadratic function as the initial function $V_0(\boldsymbol{\xi})$ (see Figure 2(a)), which and its corresponding vector field $\mathbf{f}_0(\boldsymbol{\xi})$ are as follows:

$$V_0(\boldsymbol{\xi}) = g_0(\boldsymbol{\xi}) = (\boldsymbol{\xi} - \boldsymbol{\xi}_0)^T \mathbf{P} (\boldsymbol{\xi} - \boldsymbol{\xi}_0), \quad (20a)$$

$$\mathbf{f}_0(\boldsymbol{\xi}) = -\nabla V_0(\boldsymbol{\xi}) = -2\mathbf{P} (\boldsymbol{\xi} - \boldsymbol{\xi}_0), \quad (20b)$$

where \mathbf{P} is a positive definite matrix to be optimized. It is optimized by solving the following optimization problem.

$$\min_{\mathbf{P} \succ 0} \sum_{i=1}^N \left\| -2\mathbf{P} (\boldsymbol{\xi}_i^{\text{ref}} - \boldsymbol{\xi}_0) - \dot{\boldsymbol{\xi}}_i^{\text{ref}} \right\|^2. \quad (21)$$

$\{\boldsymbol{\xi}_i^{\text{ref}}, \dot{\boldsymbol{\xi}}_i^{\text{ref}}\}_{i=1}^N$ is the reference trajectories, as indicated by the red dots in Figure 2. Through optimization, the value of $\mathbf{f}_0(\boldsymbol{\xi})$ on the reference path $\boldsymbol{\xi}_i^{\text{ref}}$ is as close as possible

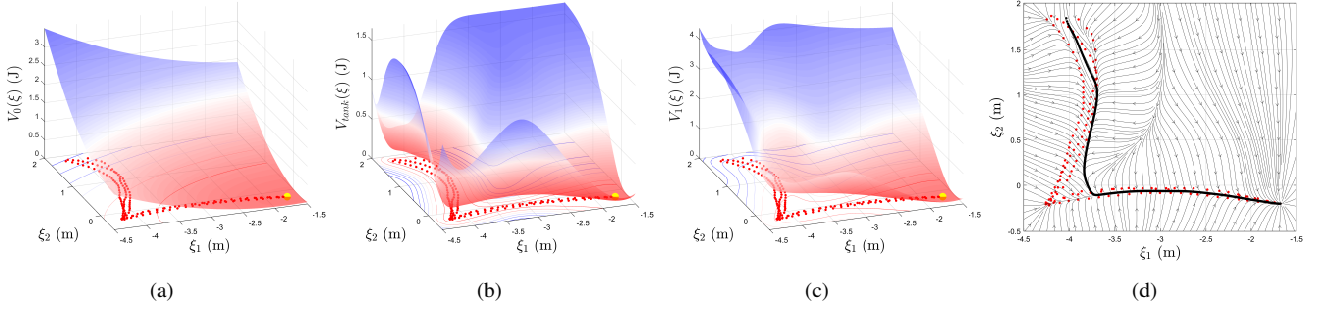


Figure 2. Schematic of integral path generation in Section 4.1. (a)-(c) show the construction process of $V_1(\xi)$. The red dots represent demonstration trajectories. (d) shows $\mathbf{f}_1(\xi) = -\nabla V_1(\xi)$, where the black curve is the integration path from the average start point of the demonstration trajectories. (a) The initial function $V_0(\xi)$. (b) The notch function $V_{\text{tank}}(\xi)$. (c) The composite function $V_1(\xi)$. (d) The vector field $\mathbf{f}_1(\xi)$ corresponding to $V_1(\xi)$.

to the reference velocity ξ_i^{ref} . The optimal \mathbf{P} is denoted as \mathbf{P}^* , and the corresponding function is expressed as $V_0^*(\xi) = (\xi - \xi_0)^T \mathbf{P}^* (\xi - \xi_0)$.

4.1.2 Generation of the Composite Function V_1

To make the vector field exhibit symmetric attraction with respect to the demonstration trajectory, we utilize the properties of GP to construct the notch function. We set all target values at the training points $\mathbf{X}_{\text{Ref}} = [\xi_1^{\text{ref}} \ \xi_2^{\text{ref}} \ \dots \ \xi_N^{\text{ref}}]$ to 1 (i.e., $\mathbf{y} = \mathbf{I}_{N \times 1}$). By the property of the squared exponential covariance function $k^\theta(\xi, \xi')$, the value of $gp(\theta, \mathbf{X}_{\text{Ref}}, \mathbf{I}_{N \times 1}, \xi)$ decays to zero as ξ moves away from the demonstration trajectories \mathbf{X}_{Ref} . Therefore, we construct the notch function $V_{\text{tank}}(\xi, a, \theta_1)$ (see Figure 2(b)) based on the following structure:

$$V_{\text{tank}} = (1 - r_a(\xi)) (1 + \varepsilon - gp(\theta_1, \mathbf{X}_{\text{Ref}}, \mathbf{I}_{N \times 1}, \xi)), \quad (22)$$

where ε is a small positive number such that the value of V_{tank} is constantly non-negative. $r_a(\xi) = \exp(-a\|\xi - \xi_0\|^2)$ is the radial basis function centered on ξ_0 . The coefficient $(1 - r_a(\xi))$ makes the values of the function V_{tank} and its derivative at ξ_0 are zero.

Based on the initial function V_0 and the notch function V_{tank} , we obtain the composite function V_1 (see Figure 2(c)):

$$\begin{aligned} V_1(\xi, a, b, \theta_1) &= g_1(\xi, a, b, \theta_1) \\ &= V_0^*(\xi) + bV_{\text{tank}}(\xi, a, \theta_1). \end{aligned} \quad (23)$$

By solving the following optimization problem, we can then obtain the values of the coefficients to be determined:

$$\begin{aligned} \min_{\{a, b, \theta_1\}} & \sum_{i=1}^N \left\| -\nabla V_1(\xi_i^{\text{ref}}, a, b, \theta_1) - \xi_i^{\text{ref}} \right\|^2 \\ \text{s.t. } & a \in [a^l, a^u], \\ & b \in [b^l, b^u], \\ & \theta_1 \in \Theta. \end{aligned} \quad (24)$$

∇V_1 can be obtained analytically for the solution of the optimization, and we will explain this in detail later. The optimal coefficients are denoted as $\{a^*, b^*, \theta_1^*\}$.

4.1.3 Generation of the Integral Path

For $\xi \in \mathbb{R}^n$, $\mathbf{X} = [\xi_1 \ \xi_2 \ \dots \ \xi_N] \in \mathbb{R}^{n \times N}$ and $\mathbf{y} \in \mathbb{R}^{N \times 1}$, the posterior mean $gp(\xi)$ and its gradient $\nabla gp(\xi)$ can be expressed as

$$gp(\xi) = K^\theta(\xi, \mathbf{X})_{1 \times N} [K^\theta(\mathbf{X}, \mathbf{X}) + \sigma_n^2 \mathbf{I}]_{N \times N}^{-1} \mathbf{y}_{N \times 1}, \quad (25a)$$

$$\nabla gp(\xi) = [K]_{1 \times N \times n} [K^\theta(\mathbf{X}, \mathbf{X}) + \sigma_n^2 \mathbf{I}]_{N \times N}^{-1} \mathbf{y}_{N \times 1}, \quad (25b)$$

where $[K]_{1 \times N \times n}$ is a third-order tensor, and its components can be expressed analytically as

$$[K]_{1ij} = \nabla_\xi K^\theta(\xi, \xi_j)_{n \times 1}. \quad (26)$$

Further, the integral vector field $\mathbf{f}_1(\xi)$ can be obtained analytically by taking the gradient of $V_1(\xi, a^*, b^*, \theta_1^*)$. The integral path which represents the geometrical features of the demonstration trajectory can be obtained by integrating over the vector field $\mathbf{f}_1(\xi)$ (see Figure 2(d)):

$$\dot{\xi} = \mathbf{f}_1(\xi) = -\nabla V_1(\xi, a^*, b^*, \theta_1^*), \quad (27a)$$

$$\left\{ \xi_i^{\text{sim}} \right\}_{i=1}^{N_s} = \text{integ}(\mathbf{f}_1(\xi), \bar{\xi}_{\text{init}}, [t_s, t_e]). \quad (27b)$$

$\bar{\xi}_{\text{init}}$ is the average starting point of the demonstration trajectories, which is used as the initial integration point.

$[t_s, t_e]$ is the integration interval. $\left\{ \xi_i^{\text{sim}} \right\}_{i=1}^{N_s}$ is the set of equally spaced sampled points (control points) on the integration path. To enhance the subsequent optimization results in Section 4.3, the reference value of the demonstration trajectory can be updated to $\left\{ \xi_i^{\text{ref}}, \xi_i^{\text{ref}} \right\}_{i=1}^{N_s} =$

$$\left\{ \xi_i^{\text{sim}}, \mathbf{f}_1(\xi_i^{\text{sim}}) \right\}_{i=1}^{N_s}.$$

Through the above process, we obtain the integral path based on GP. It is worth noting that we can obtain the integral path by other efficient methods, such as the LPV-DS $\mathbf{f}_{\text{LPV}}(\xi)$ (Figuroa and Billard 2018):

$$\left\{ \xi_i^{\text{sim}} \right\}_{i=1}^{N_s} = \text{integ}(\mathbf{f}_{\text{LPV}}(\xi), \bar{\xi}_{\text{init}}, [t_s, t_e]). \quad (28)$$

For different types of demonstration trajectories, different methods have different results. The appropriate method can be selected according to the specific case.

4.2 Construction of the Potential Function

In Section 4.1, we directly obtain the notch function $V_{\text{tank}}(\boldsymbol{\xi})$ based on the demonstration path $\{\boldsymbol{\xi}_i^{\text{ref}}\}_{i=1}^N$. Since the actual demonstration trajectory has some noise and perturbation, it is difficult for the notch function to flexibly characterize an arbitrary velocity profile $\{\boldsymbol{\xi}_i^{\text{ref}}\}_{i=1}^N$ and satisfy the stability constraints (19).

In this section, we will utilize the control points $\{\boldsymbol{\xi}_i^{\text{sim}}\}_{i=1}^{N_s}$ obtained in Section 4.1 to construct the potential energy function V_p corresponding to the target DS $\mathbf{f}_p = -\nabla_{\boldsymbol{\xi}} V_p$. $\{\boldsymbol{\xi}_i^{\text{sim}}\}_{i=1}^{N_s}$ obtained from the integration has more regular geometric features, making V_p smooth and easy to regulate.

4.2.1 Construction of the GP-Ramp Function V_2

We first introduce the construction of functions for the low-dimensional motion case $\boldsymbol{\xi} \in \mathbb{R}^2$, and for more complex cases we will present them in Section 5.

We wish the robot to move at a reference velocity along the integration path while resisting perturbation in the vertical direction of the reference velocity. To make the potential energy function more smooth and regular in the vertical direction of the reference velocity, we can expand the sampling points in that direction. We denote all control points as the matrix $\mathbf{X}_{\text{sim}} = [\boldsymbol{\xi}_1^{\text{sim}} \boldsymbol{\xi}_2^{\text{sim}} \cdots \boldsymbol{\xi}_{N_s}^{\text{sim}}]$. For each point $\boldsymbol{\xi}$ on the integration path, the corresponding velocity is $\mathbf{f}_1(\boldsymbol{\xi}) = [f_1^x(\boldsymbol{\xi}) f_1^y(\boldsymbol{\xi})]^T$, and its perpendicular direction is $\mathbf{n}(\boldsymbol{\xi}) = \frac{\mathbf{m}(\boldsymbol{\xi})}{\|\mathbf{m}(\boldsymbol{\xi})\|}$, where $\mathbf{m}(\boldsymbol{\xi}) = [-f_1^y(\boldsymbol{\xi}) f_1^x(\boldsymbol{\xi})]^T$. We denote the normal corresponding to all control points as $\mathbf{N} = [\mathbf{n}(\boldsymbol{\xi}_1^{\text{sim}}) \mathbf{n}(\boldsymbol{\xi}_2^{\text{sim}}) \cdots \mathbf{n}(\boldsymbol{\xi}_{N_s}^{\text{sim}})]$. The expanded point set (see the green dots in Figure 3(a)) can be denoted as $\mathbf{X}_{\text{SimAll}} = [\mathbf{X}_{\text{sim}}, \mathbf{X}_{\text{sim}} + \mu\mathbf{N}, \mathbf{X}_{\text{sim}} - \mu\mathbf{N}]$, where μ is a distance factor. Here, we triple the set of control points, and other expansions are also optional. In GP model, the observed target values $\mathbf{y} = [y_1 y_2 \cdots y_{N_s}]^T$ corresponding to the training points \mathbf{X}_{sim} also needs to be tripled:

$$\mathbf{y}_{\text{total}} = \begin{bmatrix} \mathbf{y} \\ \mathbf{y} \\ \mathbf{y} \end{bmatrix} = \begin{bmatrix} \mathbf{I} \\ \mathbf{I} \\ \mathbf{I} \end{bmatrix} \mathbf{y}. \quad (29)$$

The expanded target values (29) means that every three points $\{\boldsymbol{\xi}_i^{\text{sim}}, \boldsymbol{\xi}_i^{\text{sim}} + \mu\mathbf{n}(\boldsymbol{\xi}_i^{\text{sim}}), \boldsymbol{\xi}_i^{\text{sim}} - \mu\mathbf{n}(\boldsymbol{\xi}_i^{\text{sim}})\}$ correspond to the same target value y_i , as shown in Figure 3(c).

Denote $\boldsymbol{\Gamma} = [0 \ 0 \ \cdots \ 0 \ 1]_{1 \times N_s}$, then $y_{N_s} = \boldsymbol{\Gamma} \mathbf{y}$. The GP-Ramp function V_2 is constructed as follows:

$$V_2(\boldsymbol{\xi}, \boldsymbol{\theta}_2, \mathbf{y}) = (1 - r_a(\boldsymbol{\xi})) (\varepsilon + \boldsymbol{\Gamma} \mathbf{y} - V_{21}(\boldsymbol{\xi}) V_{22}(\boldsymbol{\xi}, \boldsymbol{\theta}_2, \mathbf{y})), \quad (30)$$

where

$$V_{21}(\boldsymbol{\xi}) = gp(\boldsymbol{\theta}_1, \mathbf{X}_{\text{SimAll}}, \mathbf{I}_{3N_s \times 1}, \boldsymbol{\xi}), \quad (31)$$

$$V_{22}(\boldsymbol{\xi}, \boldsymbol{\theta}_2, \mathbf{y}) = gp(\boldsymbol{\theta}_2, \mathbf{X}_{\text{SimAll}}, \mathbf{y}_{\text{total}}, \boldsymbol{\xi})$$

$$= K^{\boldsymbol{\theta}_2}(\boldsymbol{\xi}, \mathbf{X}_{\text{SimAll}}) [K^{\boldsymbol{\theta}_2}(\mathbf{X}_{\text{SimAll}}, \mathbf{X}_{\text{SimAll}}) + \sigma_n^2 \mathbf{I}]^{-1} \begin{bmatrix} \mathbf{y} \\ \mathbf{y} \\ \mathbf{y} \end{bmatrix} \mathbf{S}_i \quad (32)$$

The function V_{21} is obtained by setting all the target values \mathbf{y} to 1, as shown in Figure 3(b). V_{21} is used as a penalty

factor to make V_2 smoother on the integration path. The function V_{22} realizes the adjustment of the slope of V_2 on the integration path by modulating the corresponding target value \mathbf{y} at the control point \mathbf{X}_{sim} , as shown in Figure 3(c). The coefficient $(1 - r_a(\boldsymbol{\xi}))$ makes the values of the function V_2 and its derivative at $\boldsymbol{\xi}_0$ are zero, as shown in Figure 3(d).

By observing (30)-(32), an important fact is that V_2 is a linear function with respect to \mathbf{y} . This property will be used in the solution of subsequent optimization problem.

Considering that the objective of V_2 is to make the robot move along the integration path and stop at the equilibrium point $\boldsymbol{\xi}_0$, the following constraints on the objective value are given as $0 \leq y_1 < y_2 < y_3 < \cdots < y_{N_s-1} = y_{N_s}$. It is written in matrix form as follows:

$$\boldsymbol{\Gamma}_1 \mathbf{y} = [0 \ 0 \ \cdots \ 0 \ 1 \ -1]_{1 \times N_s} \mathbf{y} = \mathbf{0}, \quad (33)$$

$\boldsymbol{\Gamma}_2 \mathbf{y}$

$$= \begin{bmatrix} 1 & -1 & 0 & 0 & \cdots & 0 & 0 \\ 0 & 1 & -1 & 0 & \cdots & 0 & 0 \\ 0 & 0 & 1 & -1 & \ddots & \vdots & \vdots \\ \vdots & \ddots & \ddots & \ddots & \ddots & 0 & \vdots \\ 0 & \cdots & 0 & 0 & 1 & -1 & 0 \end{bmatrix}_{(N_s-2) \times N_s} \mathbf{y} < \mathbf{0}. \quad (34)$$

4.2.2 Construction of the Base Function Φ

The GP-Ramp function V_2 in Section 4.2.1 has flexible slope regulation. However, due to the property of the covariance function $k^\theta(\boldsymbol{\xi}, \boldsymbol{\xi}')$, V_2 becomes flat as $\boldsymbol{\xi}$ moves away from the demonstration trajectory, as shown in Figure 3(d). In this section, we construct the base function Φ to "attract" the distant state point $\boldsymbol{\xi}$. Moreover, the function can exhibit variable stiffness properties on the demonstration trajectory to exhibit different symmetric attractiveness for different regions.

Based on the control points $\{\boldsymbol{\xi}_i^{\text{sim}}\}_{i=1}^{N_s}$, the base function is constructed as

$$\Phi(\boldsymbol{\xi}) = \sum_{i=1}^{N_s} \tilde{\omega}_i(\boldsymbol{\xi}) \phi_i(\boldsymbol{\xi}), \quad (35)$$

where

$$\phi_i(\boldsymbol{\xi}) = \frac{1}{2} (\boldsymbol{\xi} - \boldsymbol{\xi}_i^{\text{sim}})^T \mathbf{S}_i (\boldsymbol{\xi} - \boldsymbol{\xi}_i^{\text{sim}}), \quad (36a)$$

$$\omega_i(\boldsymbol{\xi}) = \exp\left(-\frac{1}{2\delta_i^2} (\boldsymbol{\xi} - \boldsymbol{\xi}_i^{\text{sim}})^T (\boldsymbol{\xi} - \boldsymbol{\xi}_i^{\text{sim}})\right), \quad (36b)$$

$$\tilde{\omega}_i(\boldsymbol{\xi}) = \frac{\omega_i(\boldsymbol{\xi})}{\sum_{j=1}^{N_s} \omega_j(\boldsymbol{\xi})}. \quad (36c)$$

\mathbf{S}_i can be regarded as the equivalent stiffness at the control point $\boldsymbol{\xi}_i^{\text{sim}}$, and the tuning of the attraction stiffness can be realized flexibly by changing the value of \mathbf{S}_i . δ_i is the length-scale factor.

The gradient of the base function $\Phi(\boldsymbol{\xi})$ is easily derived analytically for subsequent parameter optimization and

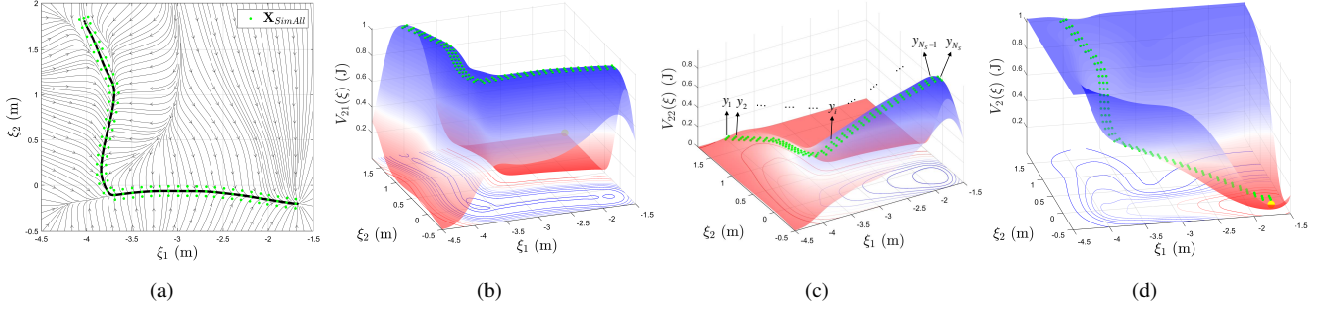


Figure 3. Schematic of GP-Ramp function $V_2(\xi)$ generation in Section 4.2.1. The green dots in (a) denote the expanded point set $\mathbf{X}_{\text{SimAll}}$ and the black line denotes the integration path. (b) and (c) are the essential functions that make up (d). (a) The expanded point set $\mathbf{X}_{\text{SimAll}}$. (b) The function $V_{21}(\xi)$. (c) The modulation function $V_{22}(\xi)$. (d) The GP-Ramp function $V_2(\xi)$.

computation of the DS:

$$\begin{aligned} \nabla\Phi(\xi) &= \sum_{i=1}^{N_s} \tilde{\omega}_i(\xi) \mathbf{S}_i(\xi - \xi_i^{\text{sim}}) \\ &\quad - \sum_{i=1}^{N_s} \frac{1}{\delta_i^2} \tilde{\omega}_i(\xi) (\phi_i(\xi) - \Phi(\xi)) (\xi - \xi_i^{\text{sim}}). \end{aligned} \quad (37)$$

4.2.3 Construction of the Total Potential Function V_p

From the previous description, base function Φ attracts the robot toward the integration (demonstration) path, and next V_2 moves the robot along the integration path at the reference velocity. Thus, the total potential function V_p (see Figure 4(a)) and the corresponding target DS \mathbf{f}_p (see Figure 4(b)) can be expressed as

$$V_p(\xi, \theta_2, \mathbf{y}) = g_p(\xi, \theta_2, \mathbf{y}) = \Phi(\xi) + V_2(\xi, \theta_2, \mathbf{y}) \quad (38a)$$

$$\mathbf{f}_p(\xi, \theta_2, \mathbf{y}) = -\nabla_{\xi} V_p(\xi, \theta_2, \mathbf{y}). \quad (38b)$$

4.3 Solution of the Optimization Problem

As can be seen from the previous subsections, the potential energy function $V_p(\xi, \theta_2, \mathbf{y})$ can be flexibly controlled by adjusting the corresponding target values \mathbf{y} at control points $\{\xi_i^{\text{sim}}\}_{i=1}^{N_s}$ as well as the hyperparameters θ_2 of the GP.

By the previous construction, $\nabla g_p(\xi_0) = \mathbf{0}$ and $g_p(\xi_0) = 0$. The stability constraints (19) are simplified to

$$g_p(\xi) > 0, \quad \xi \neq \xi_0 \quad (39a)$$

$$\|\nabla g_p(\xi)\| > 0, \quad \xi \neq \xi_0. \quad (39b)$$

The goal of the optimization is to get as much consistency as possible between the constructed DS $\dot{\xi}_i^{\text{GP}} = \mathbf{f}_p(\xi_i^{\text{ref}}, \theta_2, \mathbf{y})$

and the reference velocity $\dot{\xi}_i^{\text{ref}}$. We select the key region $\mathcal{C} \subset \mathbb{R}^n$ to impose stability constraint (39). Constraint (39) is applied to the sampled points $\{\xi_i^{\text{sam}}\}_{i=1}^{N_a}$ by sampling N_a suitable points in the region \mathcal{C} . The well-chosen sampling of points $\{\xi_i^{\text{sam}}\}_{i=1}^{N_a}$ can generalize the incorporated discrete constraints to the continuous region \mathcal{C} (Lemme et al. 2014). Combining the above description and also considering the monotonicity constraint on \mathbf{y} , the optimization problem can

be built in the following form:

$$\begin{aligned} \min_{\{\theta_2, \mathbf{y}\}} \quad & \frac{1}{N} \sum_{i=1}^N \left\| -\nabla V_p(\xi_i^{\text{ref}}, \theta_2, \mathbf{y}) - \dot{\xi}_i^{\text{ref}} \right\|^2 \\ \text{s.t.} \quad & \mathbf{\Gamma}_1 \mathbf{y} = \mathbf{0}, \\ & \mathbf{\Gamma}_2 \mathbf{y} < \mathbf{0}, \\ & g_p(\xi_j^{\text{sam}}, \theta_2, \mathbf{y}) > 0, \quad (j = 1, 2, \dots, N_a) \\ & \|\nabla g_p(\xi_j^{\text{sam}}, \theta_2, \mathbf{y})\| > 0. \quad (j = 1, 2, \dots, N_a) \end{aligned} \quad (40)$$

The objective function and constraints of the optimization problem (40) are highly nonlinear functions with respect to the optimization variables $\{\theta_2, \mathbf{y}\}$. Solving them directly is tedious and time-consuming.

Notice that V_2 is a linear function of \mathbf{y} , so V_p and its gradient $\nabla_{\xi} V_p$ are also linear functions with respect to \mathbf{y} , which can be expressed as:

$$V_p(\xi, \theta_2, \mathbf{y}) = \mathbf{a}(\xi, \theta_2) \mathbf{y} + \mathbf{b}(\xi, \theta_2), \quad (41a)$$

$$\mathbf{f}_p(\xi, \theta_2, \mathbf{y}) = -\nabla_{\xi} V_p(\xi, \theta_2, \mathbf{y}) = \mathbf{A}(\xi, \theta_2) \mathbf{y} + \mathbf{B}(\xi, \theta_2), \quad (41b)$$

where $\mathbf{a}(\xi, \theta_2)$, $\mathbf{b}(\xi, \theta_2)$, $\mathbf{A}(\xi, \theta_2)$ and $\mathbf{B}(\xi, \theta_2)$ are the coefficients of linear equations (41).

Therefore, when fixing θ_2 , the above optimization problem can be regarded as a quadratic constrained quadratic programming (QCQP) problem \mathbf{P}_1 with respect to \mathbf{y} :

$$\begin{aligned} \min_{\mathbf{y}} \quad & \frac{1}{N} \sum_{i=1}^N \left\| \mathbf{A}(\xi_i^{\text{ref}}, \theta_2) \mathbf{y} + \mathbf{B}(\xi_i^{\text{ref}}, \theta_2) - \dot{\xi}_i^{\text{ref}} \right\|^2 \\ \text{s.t.} \quad & \mathbf{\Gamma}_1 \mathbf{y} = \mathbf{0}, \\ & \mathbf{\Gamma}_2 \mathbf{y} < \mathbf{0}, \\ & \mathbf{a}(\xi_j^{\text{sam}}, \theta_2) \mathbf{y} + \mathbf{b}(\xi_j^{\text{sam}}, \theta_2) > 0, \quad (j = 1, \dots, N_a) \\ & \left\| \mathbf{A}(\xi_j^{\text{sam}}, \theta_2) \mathbf{y} + \mathbf{B}(\xi_j^{\text{sam}}, \theta_2) \right\|^2 > 0. \quad (j = 1, \dots, N_a) \end{aligned} \quad (42)$$

The above problem \mathbf{P}_1 can be solved by using the interior-point algorithm with the fmincon solver in MATLAB.

When we update \mathbf{y} by solving \mathbf{P}_1 , the hyperparameter θ_2 can be subsequently updated by minimizing the negative logarithmic marginal likelihood (NLML):

$$\min_{\theta_2} -\log p(\mathbf{y}_{\text{total}} | \mathbf{X}_{\text{SimAll}}, \theta_2). \quad (43)$$

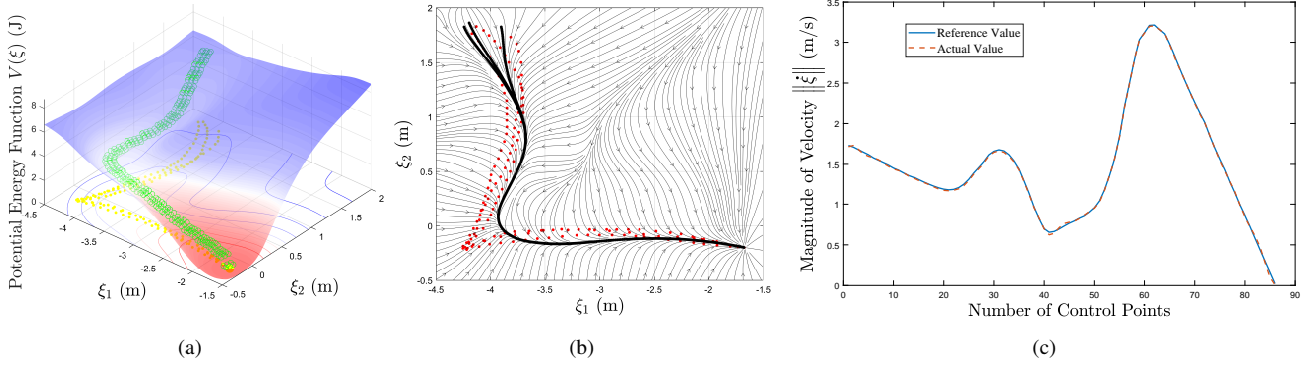


Figure 4. Simulation of DS generation on the L-shaped trajectory. The process and details of the DS generation based on GP are displayed in (a), (b) and (c). The red dots represent demonstration trajectories. (a) The total potential function V_p based on GP. (b) DS $\dot{\xi} = \mathbf{f}_p(\xi, \theta_2, \mathbf{y})$ based on GP. (c) The velocity comparison. The actual velocity represents the result of learning through the GP.

We use the GPML toolbox (Williams and Rasmussen 2006) to solve the above optimization problem (43). It is worth noting that when θ_2 is updated, the optimization model \mathbf{P}_1 (42) is also updated. Thus, the original optimization problem (40) is decomposed into an iterative optimization of the parameters \mathbf{y} and θ_2 , as shown in Figure 5. The optimization process ends when the number of iterations reaches the maximum or the change in the optimization parameters $\{\theta_2, \mathbf{y}\}$ is less than the set threshold. A series of simulation results in this paper illustrate the effectiveness of the proposed optimization method.

After optimization, the actual velocity $\dot{\xi}_i^{\text{GP}} = \mathbf{f}_p(\xi_i^{\text{ref}}, \theta_2, \mathbf{y})$ at ξ_i^{ref} is highly consistent with the reference velocity $\dot{\xi}_i^{\text{ref}}$, as shown in Figure 4(c). The above results illustrate the effectiveness of the GP-based approach.

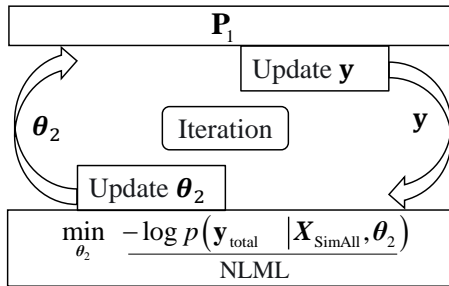


Figure 5. Schematic diagram of the iterative optimization process. Update \mathbf{y} by solving the QCQP optimization problem \mathbf{P}_1 (42) and subsequently update θ_2 by solving the optimization problem (43).

5 Generalizability of the Proposed Methodology

The method for generating conservative DS in low-dimensional flat space is presented in Section 4. In this section, we generalize the method introduced in Section 4 to make the method applicable to different manifolds as well as special motion trajectories.

5.1 The High-Dimension Space

After expanding the set of control points for the case of high-dimensional spaces, the method in Section 4 can be naturally generalized to high-dimensional linear spaces.

Similarly, we denote all control points as the matrix $\mathbf{X}_{\text{sim}} = [\xi_1^{\text{sim}} \xi_2^{\text{sim}} \cdots \xi_{N_s}^{\text{sim}}]$. For each point $\xi \in \mathbb{R}^n$ on the integration path, the corresponding velocity is $\mathbf{f}_1(\xi) \in \mathbb{R}^n$, and there exist $n-1$ linearly independent vectors in its perpendicular direction. Depending on the specific situation, l vertical vectors $\mathbf{n}_i(\xi) \perp \mathbf{f}_1(\xi)$ are selected ($i = 1, \dots, l < n-1$). We denote the normal matrix corresponding to the i th perpendicular direction as $\mathbf{N}_i = [\mathbf{n}_i(\xi_1^{\text{sim}}) \mathbf{n}_i(\xi_2^{\text{sim}}) \cdots \mathbf{n}_i(\xi_{N_s}^{\text{sim}})]$ ($i = 1, \dots, l$). Then the expanded control point set (see the green dots in Figure 6(b)) can be denoted as $\mathbf{X}_{\text{SimAll}} = [\mathbf{X}_{\text{sim}}, \mathbf{X}_{\text{sim}} + \mu\mathbf{N}_1, \dots, \mathbf{X}_{\text{sim}} + \mu\mathbf{N}_l]$. In GP model, the observed target values $\mathbf{y} = [y_1 y_2 \cdots y_{N_s}]^T$ corresponding to the training points \mathbf{X}_{sim} also needs to be expanded:

$$\mathbf{y}_{\text{total}} = \begin{bmatrix} \mathbf{y} \\ \vdots \\ \mathbf{y} \end{bmatrix}_{(l+1) \cdot N_s \times 1} = \begin{bmatrix} \mathbf{I} \\ \vdots \\ \mathbf{I} \end{bmatrix}_{(l+1) \cdot N_s \times N_s} \mathbf{y} \quad (44)$$

The expanded target values (44) means that every $l+1$ points $\{\xi_i^{\text{sim}}, \xi_i^{\text{sim}} + \mu\mathbf{n}_1(\xi_i^{\text{sim}}), \dots, \xi_i^{\text{sim}} + \mu\mathbf{n}_l(\xi_i^{\text{sim}})\}$ correspond to the same target value y_i , as shown in Figure 6(c).

For the sake of demonstration, take the 3-dimensional Cartesian space as an example, as shown in Figure 6. In this case, we select $l = 4$ for control point expansion, as shown in Figure 6(b). GP-based generated potential function still generates effective attraction regions around the demonstration path in 3D space, as shown in Figure 6(c). The initial point of motion is randomly selected, and the motion trajectory first rapidly converges to the demonstration trajectory, followed by motion to the equilibrium point. This exhibits a clear symmetric attractiveness of the GP-generated DS, as shown in Figure 6(d).

5.2 The Rotation motion

The trajectories in the aforementioned linear space \mathbb{R}^n describe translational motion. The motion of the robot

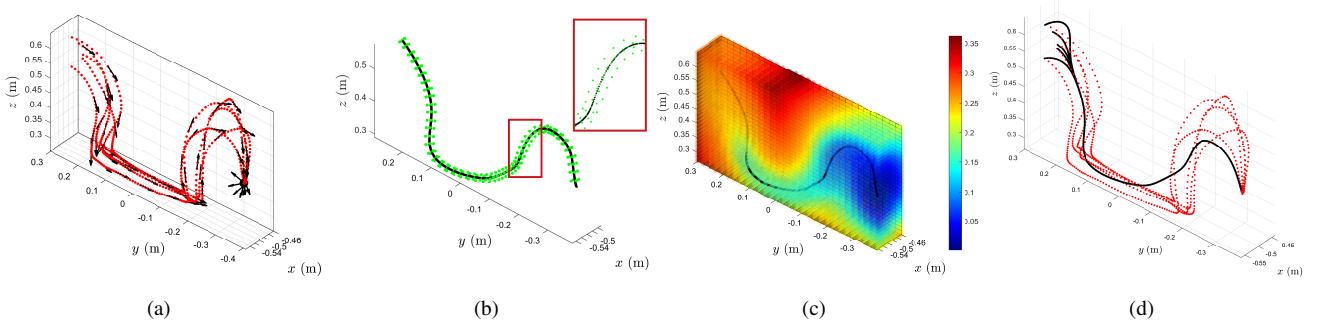


Figure 6. Schematic of the process of DS generation in high-dimensional space \mathbb{R}^3 . The red dots represent demonstration trajectories. The green dots in (b) denote the expanded point set $\mathbf{X}_{\text{SimAll}}$. (a) Reference demonstration trajectory in \mathbb{R}^3 . (b) The expanded point set $\mathbf{X}_{\text{SimAll}}$. (c) Potential energy function V_p generated in \mathbb{R}^3 . The color indicates the value of the potential energy. (d) DS generated in \mathbb{R}^3 . The black lines represent integral curves from random starting points.

system can be described as a smooth curve on the submanifold of $\text{SE}(3)$ as the system undergoes rotation. To generate a conservative DS on $\text{SE}(3)$, we first introduce the following lemma.

Lemma 4. Consistency of stiffness conservativeness (Hou et al. 2024). *A symmetric and exact joint stiffness matrix \mathbf{K}_θ always corresponds to the conservative Cartesian stiffness matrix \mathbf{K}_C on $\text{SE}(3)$.*

It follows from the Lemma 4 that we can transform the problem to generate a conservative DS in the joint space and subsequently use the kinematic (statics) relations to generate a conservative DS on $\text{SE}(3)$.

For demonstration, let's take two-degree-of-freedom rotation as an example. The posture R of the robot at any moment can be considered to be on a two-dimensional sphere S^2 . The reference trajectory of the robot can be represented as a curve on S^2 , as shown in Figure 7(b). Our goal is to generate a conservative DS $\Omega = \mathbf{f}(R)$ on S^2 , where Ω is the angular velocity. Denote the forward kinematics and differential kinematics of the robot as $fk(\cdot)$ and $d \circ fk(\cdot)$, respectively. Using the kinematic relationship, the learning from demonstration (LfD) on the original dataset $\{R_i^{\text{ref}}, \Omega_i^{\text{ref}}\}_{i=1}^N$ can be transformed into the LfD on dataset $\{\theta_i^{\text{ref}}, \dot{\theta}_i^{\text{ref}}\}_{i=1}^N$, where θ and $\dot{\theta}$ are the robot joint angles and angular velocities, respectively. At this point, the goal translates into generating conservative DS $\dot{\theta} = \mathbf{f}_\theta(\theta)$ in the linear joint space, which can be achieved based on the method in Section 4. Finally, the conservative DS $\mathbf{f}(R)$ on S^2 can be given based on $\mathbf{f}_\theta(\theta)$:

$$\mathbf{f} = (d \circ fk) \circ \mathbf{f}_\theta \circ fk^{-1}. \quad (45)$$

The above algorithm flow is shown in Figure 7(a). Figure 7(c) illustrates the conservative DS in the joint space, and the conservative DS on S^2 (see Figure 7(d)) can be further obtained based on the mapping relation (45). As can be seen from the Figure 7(d), the DS on S^2 is conservative and symmetrically attractive.

5.3 The Closed Trajectories & Self-Intersecting Trajectories

When the target trajectory is a closed or self-intersecting curve in \mathbb{R}^n , it is difficult to generate the DS by the method in Section 4 since the trajectory hardly corresponds to a single equilibrium point potential function defined on \mathbb{R}^n . However, we can transfer the problem to generate high-dimensional DS in the high-dimensional space \mathbb{R}^{n+1} .

5.3.1 Addition of Virtual Coordinates ξ_{vir}

For closed or self-intersecting trajectories ξ in the original \mathbb{R}^n space, it is difficult to find a single equilibrium point potential function V_p corresponding to them. However, we can describe this trajectory in higher dimensional space \mathbb{R}^{n+1} by adding virtual coordinates ξ_{vir} : $\xi \rightarrow (\xi, \xi_{vir})$. When introducing the virtual coordinate ξ_{vir} , we can design it as a unidirectional evolutionary coordinate on the high-dimensional space. In Figure 8(a), the original closed trajectory in the two-dimensional plane is transformed into a unidirectional advancing helix in three-dimensional space. Then this spiral trajectory is easy to find the corresponding potential function V_p using the algorithm in Section 4.

5.3.2 Generation of the DS in \mathbb{R}^{n+1}

For the increased dimensional trajectory (ξ, ξ_{vir}) , we are able to generate the corresponding potential function $V(\xi, \xi_{vir})$ using the algorithm in Section 4. Similarly, the high-dimensional DS $\mathbf{f}(\xi, \xi_{vir})$ can be calculated based on the potential function $V(\xi, \xi_{vir})$:

$$\mathbf{f}(\xi, \xi_{vir}) = -\nabla_{(\xi, \xi_{vir})} V(\xi, \xi_{vir}). \quad (46)$$

5.3.3 The projection of High-Dimensional DS

Since the actual physical coordinates of the target trajectory ξ are in \mathbb{R}^n , after generating the high-dimensional DS $\mathbf{f}(\xi, \xi_{vir})$, we need to project the high-dimensional DS onto the low-dimensional space \mathbb{R}^n . We first introduce the projection operator $\pi_{(1, \dots, n)}: \mathbb{R}^m \rightarrow \mathbb{R}^n$ as follows:

$$\pi_{(1, \dots, n)} [(\xi_1, \dots, \xi_n, \dots, \xi_m)] = (\xi_1, \dots, \xi_n). \quad (47)$$

Therefore, the projected DS $\mathbf{f}_{pro}(\xi, \xi_{vir})$ can be expressed as

$$\mathbf{f}_{pro}(\xi, \xi_{vir}) = \pi_{(1, \dots, n)} [\mathbf{f}(\xi, \xi_{vir})]. \quad (48)$$

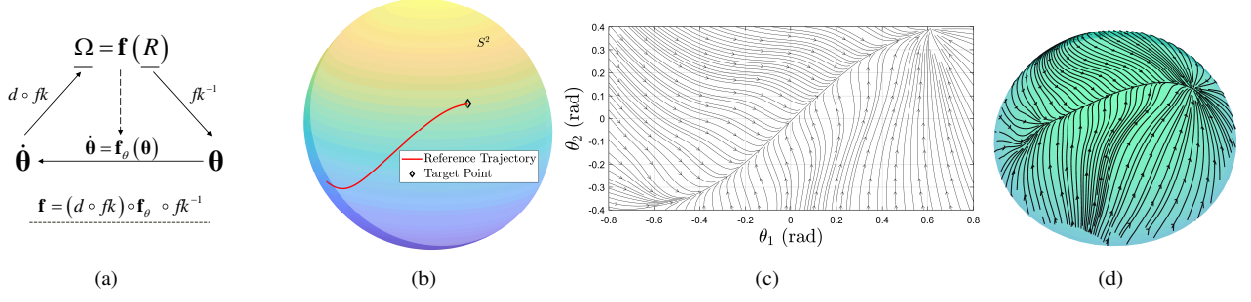


Figure 7. Schematic of the process of DS generation on S^2 . (a) Schematic diagram of the mapping relationship between joint space DS and motion manifold DS. (b) Reference demonstration trajectory on S^2 . (c) The conservative DS $\dot{\theta} = f_{\theta}(\theta)$ in the linear joint space. (d) The conservative DS $\Omega = f(R)$ on S^2 .

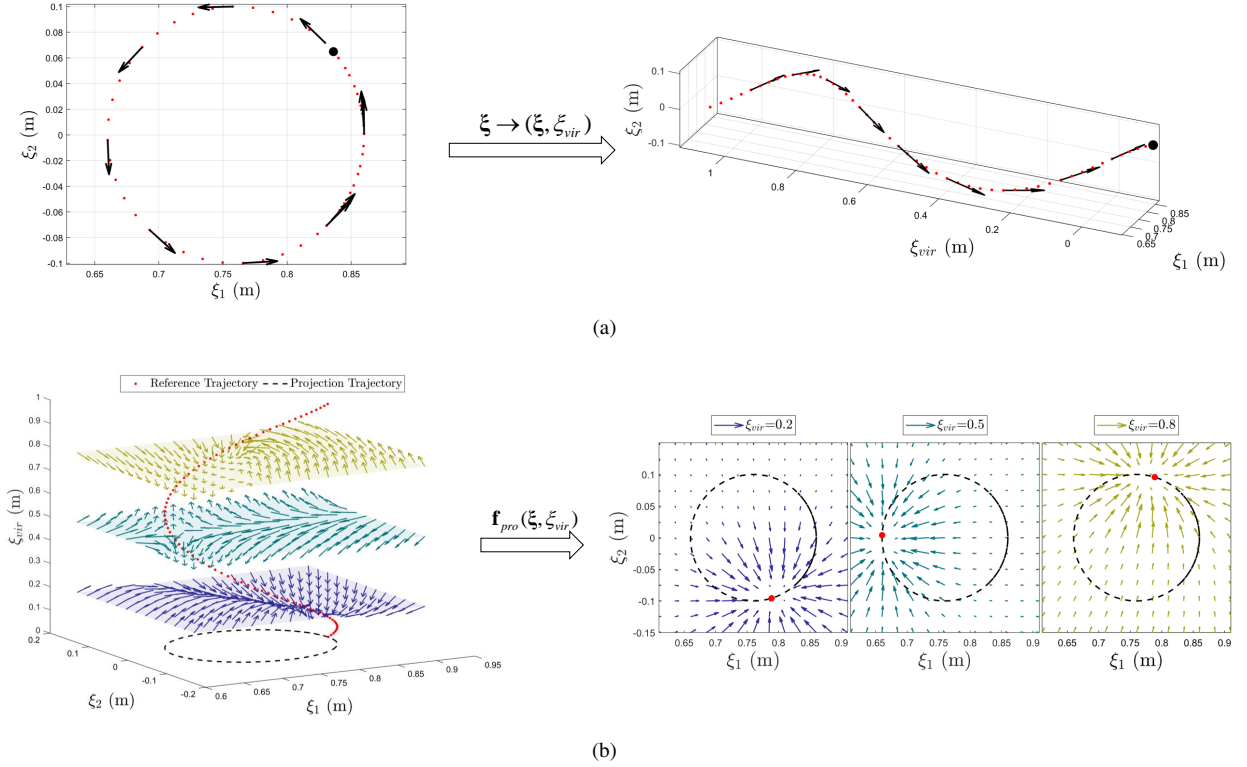


Figure 8. Schematic of the process of projected DS generation for the closed trajectories & self-intersecting trajectories. The red dots represent demonstration trajectories. The increase in spatial dimension in (a) is achieved by introducing the virtual coordinate ξ_{vir} . The three low-dimensional projected DSs corresponding to the high-dimensional DS at virtual coordinate $\xi_{vir} = [0.2, 0.5, 0.8]$ are shown in (b). (a) Schematic of dimension increase. (b) Schematic of the projection for the high-dimensional dynamical system.

In Figure 8(b), the physical space reference trajectory is shown as a black dashed line. By introducing the virtual coordinate, the reference trajectory is transformed into a red spiral line. The role of the projection operator $\pi_{(1, \dots, n)}$ is equivalent to taking the slice of the DS in 3D space corresponding to a specific virtual coordinate value.

We show three projection results for $\xi_{vir} = [0.2, 0.5, 0.8]$ in Figure 8(b). It can be seen that the two-dimensional projection DS $f_{pro}(\xi, \xi_{vir})$ exhibits a symmetric attraction about the current target point (red point), which is a result induced by the symmetric attractiveness of the DS $f(\xi, \xi_{vir})$ in the higher dimensional space. As the virtual coordinate ξ_{vir} is evolving, the equivalent target red point is constantly

changing, driving the robot to move along the closed circle trajectory in the low-dimensional space.

5.3.4 Passivity-Based Control for Projection DS

The DS obtained in the above Section 5.3.3 is finally used for the control of the robot. The impedance control based on the projected DS $f(\xi, \xi_{vir})$ is designed as follows:

$$\tau_c = G(\xi) - D(\xi, \xi_{vir})\dot{\xi} + \lambda_1 f_{pro}(\xi, \xi_{vir}), \quad (49)$$

where $D(\xi, \xi_{vir}) = Q(\xi, \xi_{vir})\Lambda Q(\xi, \xi_{vir})^T$ is the damping matrix. $Q(\xi, \xi_{vir}) = [e_1, \dots, e_n]$ is the orthogonal matrix where $e_1 = f_{pro}(\xi, \xi_{vir}) / \|f_{pro}(\xi, \xi_{vir})\|$.

The energy storage function is chosen as follows:

$$W = \frac{1}{2} \dot{\boldsymbol{\xi}}^T \mathbf{M}(\boldsymbol{\xi}) \dot{\boldsymbol{\xi}} + \lambda_1 V(\boldsymbol{\xi}, \xi_{vir}), \quad (50)$$

then we have the following proposition.

Proposition 2. *The system (1) controlled by (49) is passive with regard to the input-output pair $(\dot{\boldsymbol{\xi}}, \boldsymbol{\tau}_e)$ with the storage function (50). See Appendix B for details.*

5.4 The Decomposition of Dynamical System

In the above sections, we introduced learning conservative DS from various demonstration trajectories. However, existing advanced methods often generate a broader class of non-conservative DS. For some cases, DS described using (polynomial) analytic expressions meet the task requirements well but tend to be non-conservative. The non-conservativeness of DS can cause the energy tanks to decay fast. Therefore, we propose an effective vector field decomposition strategy for non-conservative DS.

For any $\mathbf{f}(\boldsymbol{\xi})$, there are infinitely many ways to decompose it into a conservative part $\mathbf{f}_c(\boldsymbol{\xi})$ and a non-conservative part $\mathbf{f}_{nc}(\boldsymbol{\xi})$:

$$\mathbf{f}(\boldsymbol{\xi}) = \mathbf{f}_c(\boldsymbol{\xi}) + \mathbf{f}_{nc}(\boldsymbol{\xi}). \quad (51)$$

However, a superior decomposition exists for a particular design of controller.

We use the computationally convenient polynomial function $\hat{\mathbf{f}}_\nu(\boldsymbol{\xi}) = \mathbf{f}_c(\boldsymbol{\xi})$ (ν is the hyperparameters) as the conservative part. For the linear 3D spatial case $\boldsymbol{\xi} = [\xi_1 \ \xi_2 \ \xi_3]^T \in \mathbb{R}^3$, the simplest class of $\hat{\mathbf{f}}_\nu(\boldsymbol{\xi})$ is given as

$$\hat{\mathbf{f}}_\nu(\boldsymbol{\xi}) = \mathbf{f}_\nu(\boldsymbol{\xi}) - \mathbf{f}_\nu(\boldsymbol{\xi}_0), \quad (52)$$

where

$$\mathbf{f}_\nu(\boldsymbol{\xi}) = \begin{bmatrix} \nu_1(\xi_1)^4/4 + \nu_2(\xi_1)^3/3 + \nu_3(\xi_1)^2/2 + \nu_4\xi_1 \\ \nu_5(\xi_2)^4/4 + \nu_6(\xi_2)^3/3 + \nu_7(\xi_2)^2/2 + \nu_8\xi_2 \\ \nu_9(\xi_3)^4/4 + \nu_{10}(\xi_3)^3/3 + \nu_{11}(\xi_3)^2/2 + \nu_{12}\xi_3 \end{bmatrix}. \quad (53)$$

See Appendix C for specific details.

Sampling N_d points $\{\boldsymbol{\xi}_i\}_{i=1}^{N_d}$ uniformly in the critical region \mathcal{C} , one of the most direct indexes can be expressed as

$$\min_{\nu} J_1(\nu) = \frac{1}{N_d} \sum_{i=1}^{N_d} \left\| \hat{\mathbf{f}}_\nu(\boldsymbol{\xi}_i) - \mathbf{f}(\boldsymbol{\xi}_i) \right\|^2. \quad (54)$$

(54) shows that we utilize $\hat{\mathbf{f}}_\nu(\boldsymbol{\xi})$ to fit the conservative component of the original DS $\mathbf{f}(\boldsymbol{\xi})$. However, this decomposition does not fully utilize the structure of the controller and tends to be ineffective in some cases.

We analyze the passivity of the controller (2) in terms of the following energy storage function

$$W = \frac{1}{2} \dot{\boldsymbol{\xi}}^T \mathbf{M}(\boldsymbol{\xi}) \dot{\boldsymbol{\xi}} + \lambda_1 V_{f_c}(\boldsymbol{\xi}), \quad (55)$$

where $V_{f_{nc}}(\boldsymbol{\xi})$ is the potential function corresponding to $\mathbf{f}_c(\boldsymbol{\xi})$: $\mathbf{f}_c(\boldsymbol{\xi}) = -\nabla V_{f_c}(\boldsymbol{\xi})$.

Combined with the rigid body dynamics equation (1), we can obtain the rate of change of the energy storage function:

$$\begin{aligned} \dot{W} &= \dot{\boldsymbol{\xi}}^T \mathbf{M}(\boldsymbol{\xi}) \ddot{\boldsymbol{\xi}} + \frac{1}{2} \dot{\boldsymbol{\xi}}^T \dot{\mathbf{M}}(\boldsymbol{\xi}) \dot{\boldsymbol{\xi}} + \lambda_1 \nabla V_{f_c}(\boldsymbol{\xi})^T \dot{\boldsymbol{\xi}} \\ &= \dot{\boldsymbol{\xi}}^T \left(\boldsymbol{\tau}_c + \boldsymbol{\tau}_e - \mathbf{C}(\boldsymbol{\xi}, \dot{\boldsymbol{\xi}}) \dot{\boldsymbol{\xi}} - \mathbf{g}(\boldsymbol{\xi}) \right) \\ &\quad + \frac{1}{2} \dot{\boldsymbol{\xi}}^T \dot{\mathbf{M}}(\boldsymbol{\xi}) \dot{\boldsymbol{\xi}} + \lambda_1 \nabla V_{f_c}(\boldsymbol{\xi})^T \dot{\boldsymbol{\xi}} \\ &= \frac{1}{2} \dot{\boldsymbol{\xi}}^T (\dot{\mathbf{M}} - 2\mathbf{C}) \dot{\boldsymbol{\xi}} - \dot{\boldsymbol{\xi}}^T \mathbf{D} \dot{\boldsymbol{\xi}} + \dot{\boldsymbol{\xi}}^T \boldsymbol{\tau}_e \\ &\quad + (\lambda_1 \dot{\boldsymbol{\xi}}^T \mathbf{f}(\boldsymbol{\xi}) + \lambda_1 \nabla V_{f_c}(\boldsymbol{\xi})^T \dot{\boldsymbol{\xi}}) \\ &= \left(-\dot{\boldsymbol{\xi}}^T \mathbf{D} \dot{\boldsymbol{\xi}} + \lambda_1 \dot{\boldsymbol{\xi}}^T \mathbf{f}_{nc}(\boldsymbol{\xi}) \right) + \dot{\boldsymbol{\xi}}^T \boldsymbol{\tau}_e. \end{aligned} \quad (56)$$

Notice the term $\left(-\dot{\boldsymbol{\xi}}^T \mathbf{D} \dot{\boldsymbol{\xi}} + \lambda_1 \dot{\boldsymbol{\xi}}^T \mathbf{f}_{nc}(\boldsymbol{\xi}) \right)$ in (56), so the energy tank is set as (11b) and (13b).

From the energy rate equation (13b), we can slow down the dissipation of the energy s by minimizing $\dot{\boldsymbol{\xi}}^T \mathbf{f}_{nc}(\boldsymbol{\xi})$. In general, it is assumed that the actual velocity of the robot $\dot{\boldsymbol{\xi}}$ tracks well the reference velocity $\mathbf{f}(\boldsymbol{\xi})$ given by the controller. Thus We have $\dot{\boldsymbol{\xi}}^T \mathbf{f}_{nc}(\boldsymbol{\xi}) \approx \mathbf{f}(\boldsymbol{\xi})^T (\mathbf{f}(\boldsymbol{\xi}) - \hat{\mathbf{f}}_\nu(\boldsymbol{\xi}))$. The composite index after considering the controller structure is finally expressed as (corresponding to the specific energy tank design (13b))

$$\begin{aligned} \min_{\nu} J_2(\nu) &= \omega_1 \frac{1}{N_d} \sum_{i=1}^{N_d} \left\| \hat{\mathbf{f}}_\nu(\boldsymbol{\xi}_i) - \mathbf{f}(\boldsymbol{\xi}_i) \right\|^2 \\ &\quad + \omega_2 \frac{1}{N_d} \sum_{i=1}^{N_d} \mathbf{f}(\boldsymbol{\xi}_i)^T (\mathbf{f}(\boldsymbol{\xi}_i) - \hat{\mathbf{f}}_\nu(\boldsymbol{\xi}_i)), \end{aligned} \quad (57)$$

where $\boldsymbol{\omega} = [\omega_1, \omega_2]$ is the weight vector. The validity of this index will be discussed and analyzed in Section 6.3. The design of the energy tank-based controller is not unique, and for other structures, the corresponding decomposition indexes can be designed according to the above process as well.

6 Simulation and Experimental Verification

A series of simulations and experiments are conducted in this section to validate the methods proposed in Section 4 and Section 5. In Section 6.1, we test the proposed method on the classical LASA handwriting dataset (Khansari-Zadeh and Billard 2011) to highlight the symmetric attractiveness and conservativeness of the proposed method. Next, environmental obstacles are imposed during the execution of robotic arm movements to verify the interaction safety in the framework of DS in Section 6.2. Subsequently, the effectiveness of the DS decomposition is verified in Section 6.3 on more complex and twisted trajectories. Finally, for more specific closed & self-intersecting trajectories, the effectiveness of the DS decomposition is limited. Section 6.4 demonstrates that the proposed method (projection conservative DS) still handles such cases well. The above experiments illustrate that the proposed method effectively improves the stability margin during control while having the potential to handle a wide range of scenarios.

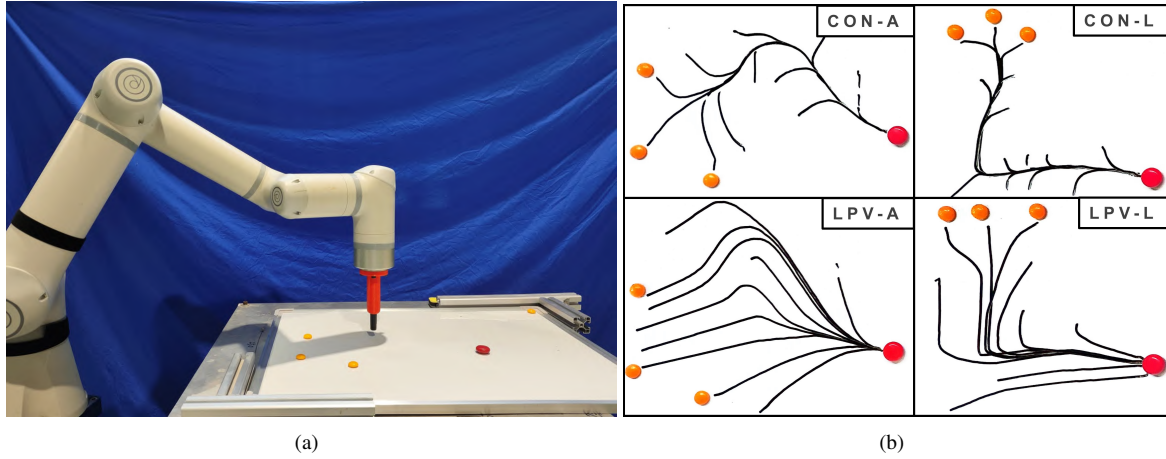


Figure 9. Schematic diagram of the experiment in Section 6.1. For clarity, the orange circle on the whiteboard indicates the start of the movement and the red circle indicates the end. (b) shows the comparative results of two different methods on two trajectories. (a) Experimental setup. (b) Experimental comparison results on the whiteboard.

6.1 LASA Handwriting Motions

The symmetric attraction and conservativeness of the DS generated in Section 4 are important in the actual motion execution. In this section, we illustrate this by performing a series of simulations and experiments on the LASA handwriting dataset.

Figure 9 illustrates the experimental setup. The experiment was conducted on a 6-DOF collaborative robot. The robot is equipped with encoders and torque sensors to acquire joint position signals and joint torque, respectively. The communication between the upper computer and the robot is realized through TwinCAT 3 interface at 1 kHz. To clearly show the robot’s trajectory, we mounted a pen on the end of the robot arm and used a whiteboard to record the trajectory during the movement. Also, the orange circles were used to indicate the starting point of the motion, and a red circle was used to indicate the equilibrium point ξ_0 corresponding to the DS.

Using the method in Section 4, we generated the DS corresponding to the A-shaped trajectory, as shown in Figure 10(a), 10(b) and 10(c). Based on GP, we generated the potential energy function V_p corresponding to the A-shaped demonstration trajectory in Figure 10(a). By calculating the negative gradient for V_p , we then obtain the corresponding DS in Figure 10(b). With the optimization in Section 4.3, the actual velocities of the vector field generated in Figure 10(b) are highly consistent with the reference velocities and a good fit is achieved, as shown in Figure 10(c). To illustrate the role of symmetric attraction on the improvement of trajectory accuracy and perturbation resistance, we simultaneously show the DS generated based on the LPV-DS method for the same A-shaped trajectory in Figure 10(d). As can be seen in Figure 10(b), due to the symmetric attractiveness of the proposed method, after the three initial starting points are selected, the trajectories are first attracted to the demonstration trajectory quickly and then move along the demonstration trajectory to the equilibrium point.

Figure 9(b) shows the results of the whiteboard experiments in which the robot uses the proposed method in this paper and the LPV-DS method for A-shaped and

L-shaped trajectories, respectively. It can be seen that, not only for the perturbation of the start point, but also after perturbations on various intervals on the path, the proposed method (CON-A, CON-L) enables the robot to quickly return to the demonstration trajectory, and subsequently continue to execute the motion. Through the above discussion, we demonstrate the symmetric attractiveness of the approach proposed in this paper with its importance.

In Section 3, we introduce that a conservative DS corresponds to the passivity of the control system. When the DS is non-conservative, the system is kept passive by introducing the energy tank. However, when the energy s in the energy tank is depleted, the performance of the controller is affected in the following two cases: (1) the energy is depleted and the switching function $\beta(\xi, s)$ is set to zero, at which time the system has difficulty moving along the target DS $f(\xi)$ but moves along the conservative part $f_c(\xi)$; and (2) the energy tank is switched between fast charging and discharging, and the switching function $\beta(\xi, s)$ varies rapidly between zero and non-zero, which degrades the system dynamic performance.

To illustrate the importance of conservativeness for the controller, a non-conservative DS is generated based on the LPV for the A-shaped trajectory. The result is observed in simulation to show the system’s performance after energy depletion, as shown in Figure 11. The controller frequency is set to 1000 Hz in the simulation, which is consistent with the actual physical system.

Figure 11(a) illustrates the energy evolution in the energy tank, which is depleted around 1.8 s due to the presence of the non-conservative component. Subsequently, due to the charging term $\dot{\xi}^T D(\xi) \dot{\xi}$ in (13b), the energy tank switches between fast charging and discharging, which is shown as the oscillation in Figure 11(a). The oscillation of the energy s leads to a rapid change in the switching function $\beta(\xi, s)$, which, according to the controller (13a), directly leads to an oscillation of the control torque, as shown in Figure 11(d). In actual physical systems, controlling torque oscillations can lead to torque divergence, often creating serious safety hazards. Therefore, the energy s

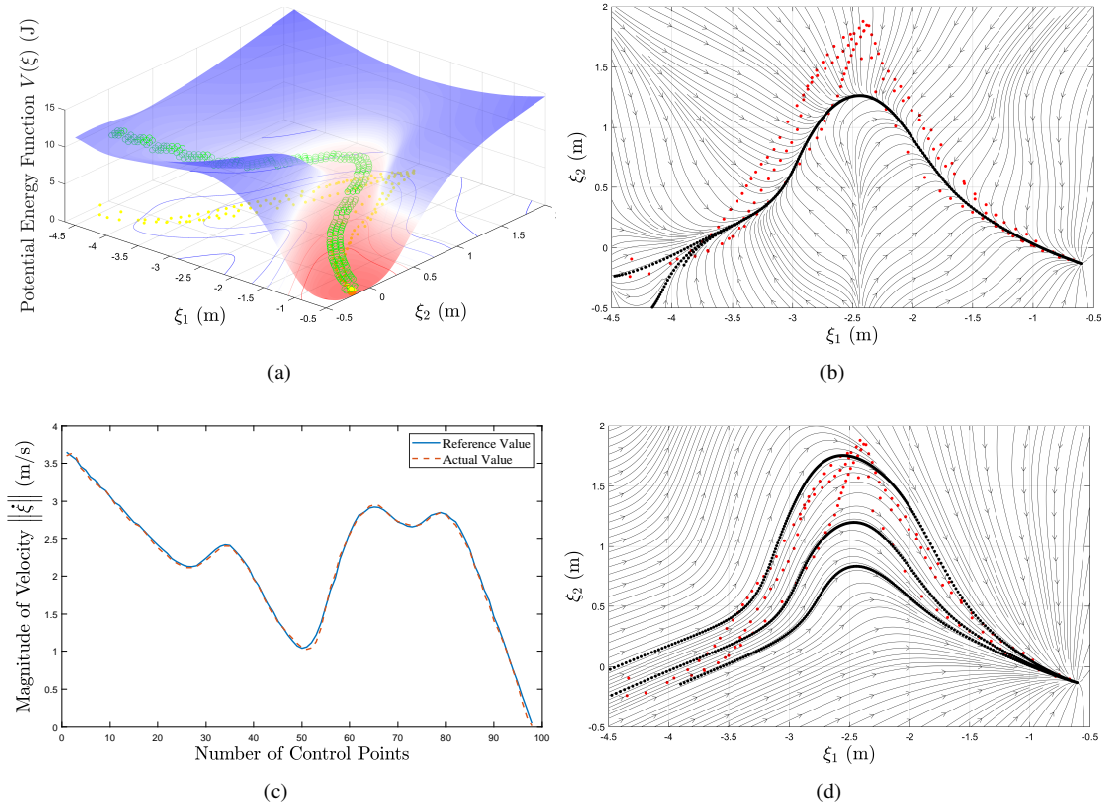


Figure 10. Simulation of DS generation on the A-shaped trajectory. The process and details of the DS generation based on GP are displayed in (a), (b) and (c). To exemplify the property of symmetric attraction, (d) shows the LPV-DS as a comparison. The red dots and black lines in (b) and (d) represent the demonstration trajectories and integral curves of DS, respectively. (a) The potential function V_p based on GP. (b) DS based on GP. (c) The velocity comparison. The actual velocity represents the result of learning through the GP. (d) LPV-DS for A-shaped trajectory.

should be avoided depletion. Although the position signal did not produce significant oscillations (see Figure 11(b)), the oscillations in torque resulted in obvious oscillations in robot velocity (see Figure 11(c)). Thus, energy depletion affects the dynamic performance of the robotic system. The DS proposed in Section 4 of this paper is conservative and therefore does not consume energy s and lead to oscillations in the signal. With the above discussion, we illustrate the importance of DS conservativeness (or DS decomposition) on the performance of control systems.

6.2 Safety in Interaction Task

In this section, we show that the DS framework exhibits interaction safety when the robot has a sudden collision with the environment. The details of the experimental setup are shown in Figure 12. A force sensor equipped at the end of the robot is used to detect the real-time interaction force as shown in Figure 12(a). The obstacles are placed on the experimental platform. The DS $f(\xi)$ designed in the experiment is shown in Figure 12(b), and the reference trajectory is a vertical downward straight line crossing the obstacle.

In the experiment, in order to detect the interaction of the robot with the environment at different collision velocities, we control the robot using a variable magnitude DS $\lambda f(\xi)$, where λ is the gain coefficient. We set up four different experimental conditions $\lambda = 0.8, 1, 1.2, 1.5$, and the robot

starts moving from the same height in each test, and the height profile of the robot end is shown in Figure 13(a). The higher the gain coefficient λ , the larger the velocity of the vector field $f(\xi)$, the faster the robot's height decreases, and the larger the interaction force between the robot and the environment according to the controller (13a). As shown in Figure 13(a), as the gain coefficient increases, the slope of the descent curve is larger and the robot is stabilized at a lower height due to the larger interaction forces. Figure 13(b) demonstrates the interaction safety for different parameters with fast stabilization of constant interaction force after the robot collides with the environment. This is because when the robot stops after a collision with the environment, the torque value of the Passive-DS controller (2) in the DS framework depends only on the current state ξ of the robot. Notice that, unlike conventional impedance control, when the robot stops due to an obstacle, the error between the actual and the reference positions gradually increases, leading to an increasing interaction force.

6.3 Dynamical System Decomposition

In practical applications and research, non-conservative DS is often widely used in trajectory generation and impedance control. However, due to the non-conservative property of DS, the performance of the controller suffers limitations when the energy tank is depleted. As shown in Section 5.4, a reasonable DS decomposition avoids depletion of the

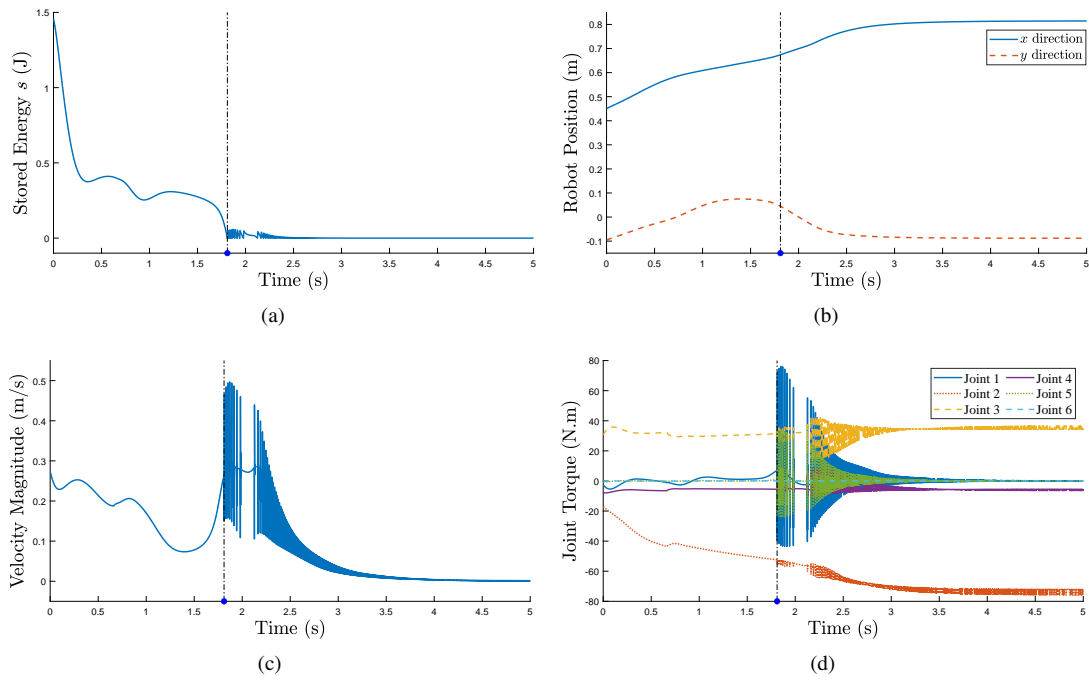


Figure 11. Simulation of LPV-DS on the A-shaped trajectory under passive-DS controller. In all figures, the black dash-dot line indicates the moment when the energy of the energy tank is depleted. (a) Schematic diagram of the energy change curve of the energy tank. (b) The 2D position profile of robot end-effector. (c) The velocity profile of robot end-effector. (d) Schematic diagram of robot joint torque.

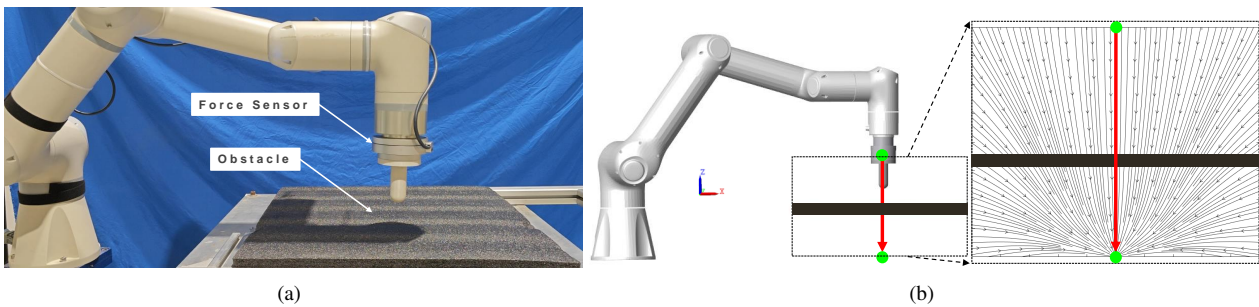


Figure 12. Schematic diagram of the experiment in Section 6.2. (a) Experimental setup. (b) The schematic of the DS setup in the experiment.

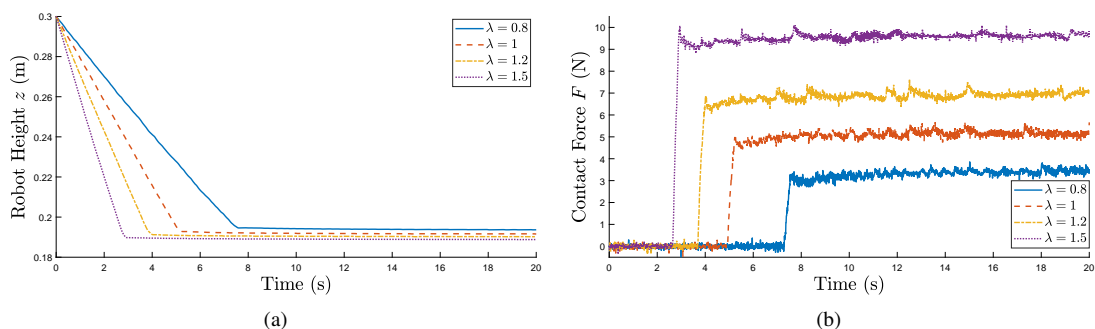


Figure 13. Schematic of the results of the interaction task experiment. In the experiment, the robot collided with the environment at four different velocities. (a) The profile of robot end-effector height change. (b) The profile of robot-environment interaction force.

energy tank and ensures the controller's performance while maintaining passivity. To illustrate the validity of the

proposed decomposition index in Section 5.4, we validate it through a series of experiments.

The experimental setup is the same as in Section 6.1, where we learn a non-conservative DS based on the LPV method on a snake-shaped demonstration trajectory as shown in Figure 14(a). The twisted character of the snake-shaped trajectory makes the generated DS strongly nonlinear, which is helpful to illustrate the effectiveness of the decomposition method. We have chosen four representative motion starting points to show that the vector field decomposition is valid for different motion paths. As shown in Figure 14(b), the four different starting points correspond to four motion paths. During the motion, we observe the change of energy s in the energy tank in real time.

To show the DS decomposition more clearly, we use the pseudocolor plot to show more information. Figure 15 shows the pseudocolor plot of the DS in Figure 14(a), and the color of each point in the plot indicates the magnitude of the angular velocity of the 2D vector field. Since the DS before decomposition is non-conservative, the colors show that the angular velocity in space is nonzero.

We first decompose the vector field using the most intuitive index (54), when the weight vector is $\omega = [1, 0]$. The conservative part and the non-conservative part are shown in Figure 16(a) and Figure 16(b), respectively. The angular velocity of the conservative part is constant and equal to zero in space.

Further, we take the controller structure into account by choosing $\omega = [1, 1]$ and using the index (57) for the decomposition. The decomposed conservative and non-conservative parts are shown in Figure 16(c) and Figure 16(d), respectively.

It is worth noting that the vector field streamlines in Figure 16(b) and Figure 16(d) are different, which means that different decompositions correspond to different conservative and non-conservative parts. However, for the two-dimensional vector field, the angular velocity of the non-conservative part after different ways of decomposition is fixed. Figure 15, Figure 16(b) and Figure 16(d) all have the same pseudocolor distribution. See Appendix D for the details.

In the experiment, we performed the experiments under three cases: 1) DS without decomposition. 2) Using the decomposition strategy $\omega = [1, 0]$. 3) Using the decomposition strategy $\omega = [1, 1]$. For each case, the robots move along the four paths in Figure 14(b) while the energy change in the energy tank is recorded as shown in Figure 17. The parameters of the energy tank are set to $[s^l, s^u] = [0, 5]$ (unit: J).

In Figure 17(a), since the DS is not decomposed, the non-conservative part $\mathbf{f}_{nc}(\xi)$ leads to a rapid energy depletion rate \dot{s} , and the energy curves corresponding to the four paths decrease rapidly.

In Figure 17(b), when the decomposition index (54) is used, the energy consumption rate decreases, and there is also an energy charging. This is because through rational decomposition, at some moments, the charging rate $\xi^T \mathbf{D}(\xi) \dot{\xi}$ in (13b) is greater than the consumption rate $\xi^T \mathbf{f}_{nc}(\xi)$. At this time, the energy curves corresponding to all four pathways decrease more slowly than those in Figure 17(a).

In Figure 17(c), after using the decomposition strategy $\omega = [1, 1]$, the energy decreases at a slower rate compared to Figure 17(b), and most of the energy curves are finally maintained at the upper limit s^u .

Through the above discussion, we illustrate the rationality and effectiveness of the decomposition index. In particular, the index J_2 (57) by considering the controller structure makes the decomposition more effective.

6.4 Dynamical Systems for Closed & Self-intersecting Motions

In Section 5.3, we discuss the DS generation method for closed & self-intersecting motions. In Section 6.4.1, we verify the validity of the method on planar motion. Further, the superiority of the proposed method over other methods is verified on curved surface motion in Section 6.4.2.

6.4.1 Motion on the Plane

We introduce the generation process of the projection DS using the closed circle trajectory in Section 5.3 as an example, as shown in Figure 18.

With the elevated dimension operation in Figure 8(a), the reference trajectory in the high-dimensional space is shown as the spiral in Figure 18(a), and the trajectory between the two red dots corresponds to the circular trajectory in the low dimension. The potential energy function $V(\xi, \xi_{vir})$ in Figure 18(b) is obtained by the iterative optimization process in Figure 5. From Figure 18(b), we can see that the potential energy $V(\xi, \xi_{vir})$ at the demonstration path is much lower than that in other regions. Meanwhile, the potential energy decreases along the demonstration path and reaches the lowest potential energy at the equilibrium point ξ_0 . The difference in potential energy leads to the symmetric attractiveness of the generated DS, as shown in Figure 18(c), where the black lines indicate the integration curves corresponding to different starting points. It should be noted that the projection DS $\mathbf{f}_{pro}(\xi, \xi_{vir})$ is finally obtained by the projection operation of Figure 8(b). The velocity corresponding to the learned DS is shown in Figure 18(d) to be in good agreement with the reference velocity.

Further, we perform experimental validation based on the projection DS $\mathbf{f}_{pro}(\xi, \xi_{vir})$. The experimental setup is the same as in Section 6.1. We generate the projection DS $\mathbf{f}_{pro}(\xi, \xi_{vir})$ based on the circle reference trajectory and the figure-of-eight reference trajectory, respectively. For the figure-of-eight self-intersecting trajectory, the DS generation process is the same as in Figure 18(c).

Figure 19(a), Figure 19(b), and Figure 19(c) demonstrate the experimental results for the circle demonstration trajectory. During the experiment, perturbations were applied by frequent human drags. Figure 19(a) shows the robot's trajectory on the whiteboard. Thanks to the symmetric attractiveness, the DS is extremely resistant to perturbations. Figure 19(b) shows the robot motion position data (x, y) collected in the experiment. It can be seen that the actual robot execution trajectory is consistent with the ideal reference circle, and the slight difference comes from the friction between the robot and the whiteboard, as well as other disturbances. To visualize the projection DS, Figure 19(c) shows the trajectory evolution of the system in high-dimensional space (x, y, w) . The dynamical

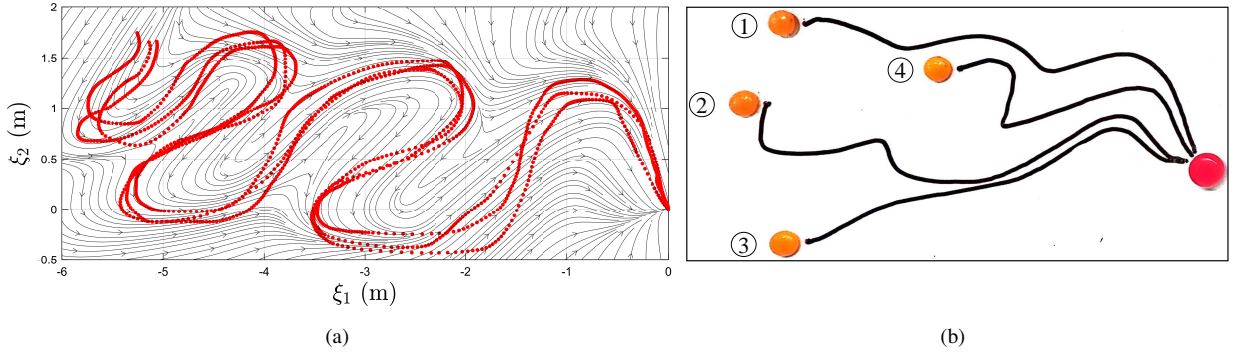


Figure 14. Schematic of the original (pre-decomposition) DS in Section 6.3. In the experiment the robot started from four fixed starting points (orange circles) while observing the consumption of energy s in the energy tank. (a) DS corresponding to the snake trajectory. The red dots represent demonstration trajectories. (b) Schematic of the four integral paths corresponding to the DS on the whiteboard.

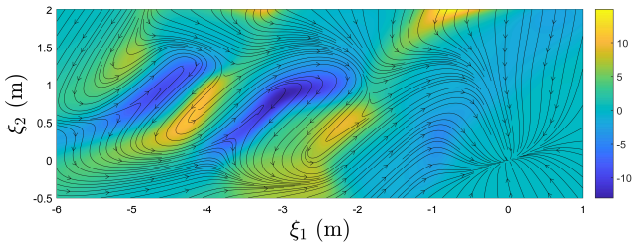


Figure 15. Schematic of the original (pre-decomposition) DS in Section 6.3. The color of each point in the figure indicates the value of the angular velocity of the vector field at the corresponding point.

system exhibits symmetric attraction with respect to the high-dimensional spiral curve, and when perturbed, the system converges along the spiral, which is visualized as convergence to the circular path in the actual physical space (x, y) . Figures 19(d) and 19(e) demonstrate the experimental results for the figure-of-eight demonstration trajectory. For this self-intersecting trajectory, the experimental results show that the proposed projection DS has an excellent anti-perturbation capability while guaranteeing path accuracy. At the same time, Proposition 2 ensures the passivity of the system under the control of the projection DS $\mathbf{f}_{pro}(\xi, \xi_{vir})$, which facilitates the realization of safe and reliable interaction tasks.

6.4.2 Motion on the Surface

In this section, we study the scenario as a robot performing closed motion on a curved surface. The experimental setup is shown in Figure 20(a), with the robot moving on a spherical surface. The sphere center is $\mathbf{p}_o = [x_o \ y_o \ z_o]^T$. We want the robot to be in contact with the surface as it moves tangentially along the surface. Therefore, the DS can be designed as follows:

$$\mathbf{f}(\xi) = \mathbf{f}_t(\xi) + \mathbf{f}_n(\xi), \quad (58)$$

where $\mathbf{f}_t(\xi)$ is the nominal DS that performs the surface motion and $\mathbf{f}_n(\xi)$ is the normal modulation DS that keeps the robot in contact with the surface, as shown in Figure 20(b).

The normal modulation DS $\mathbf{f}_n(\xi)$ is always perpendicular to the surface:

$$\mathbf{f}_n(\xi) = \frac{F_d}{\lambda_1} \mathbf{n}(\xi), \quad (59)$$

where F_d is the expected contact force and $\mathbf{n}(\xi)$ is the surface normal.

As shown by the red dashed line in Figure 20(b), the circle on the sphere with center $\mathbf{p}_c = [x_c \ y_c \ z_c]^T$ and radius $r = 0.1$ m was chosen as the reference trajectory in the experiment. We first define the following DS describing the circular motion:

$$\mathbf{f}_{cir}(\xi) = \begin{pmatrix} v_t (r - R) x - v_w y \\ v_t (r - R) y + v_w x \\ v_z (z_c - z) \end{pmatrix}, \quad (60a)$$

$$R = \sqrt{(x - x_c)^2 + (y - y_c)^2}, \quad (60b)$$

where $\xi = [x \ y \ z]^T$ is the robot end position. v_t , v_w and v_z denote the normal, tangential and z -direction velocity coefficients, respectively.

The nominal DS $\mathbf{f}_t(\xi)$ is constructed as follows:

$$\mathbf{f}_t(\xi) = v_0 \frac{\hat{\mathbf{f}}_{cir}(\xi)}{\|\hat{\mathbf{f}}_{cir}(\xi)\|}, \quad (61a)$$

$$\hat{\mathbf{f}}_{cir}(\xi) = \mathbf{f}_{cir}(\xi) - (\mathbf{n}^T(\xi) \mathbf{f}_{cir}(\xi)) \mathbf{n}(\xi), \quad (61b)$$

where v_0 denotes the magnitude of the tangential velocity of the end-effector. In this experiment, set $F_d = 5$ N and $v_0 = 0.1$ m/s.

Since the modulated DS can be considered conservative, we next focus on the analysis of the nominal DS. The pseudocolor plot of the nominal DS $\mathbf{f}_t(\xi)$ is illustrated in Figure 20(c). It can be seen that the angular velocity of $\mathbf{f}_t(\xi)$ is not constant zero and is therefore non-conservative.

Since the nominal DS (61) is non-conservative, the depletion of energy in the energy tank is slowed down by decomposing it. Similar to Section 6.3, we use the decomposition strategies $\omega = [1, 0]$ and $\omega = [1, 1]$, which correspond to the decomposition index (54) and index (57), respectively. The result of the decomposition is shown in Figure 21, where it can be seen that the angular velocity of

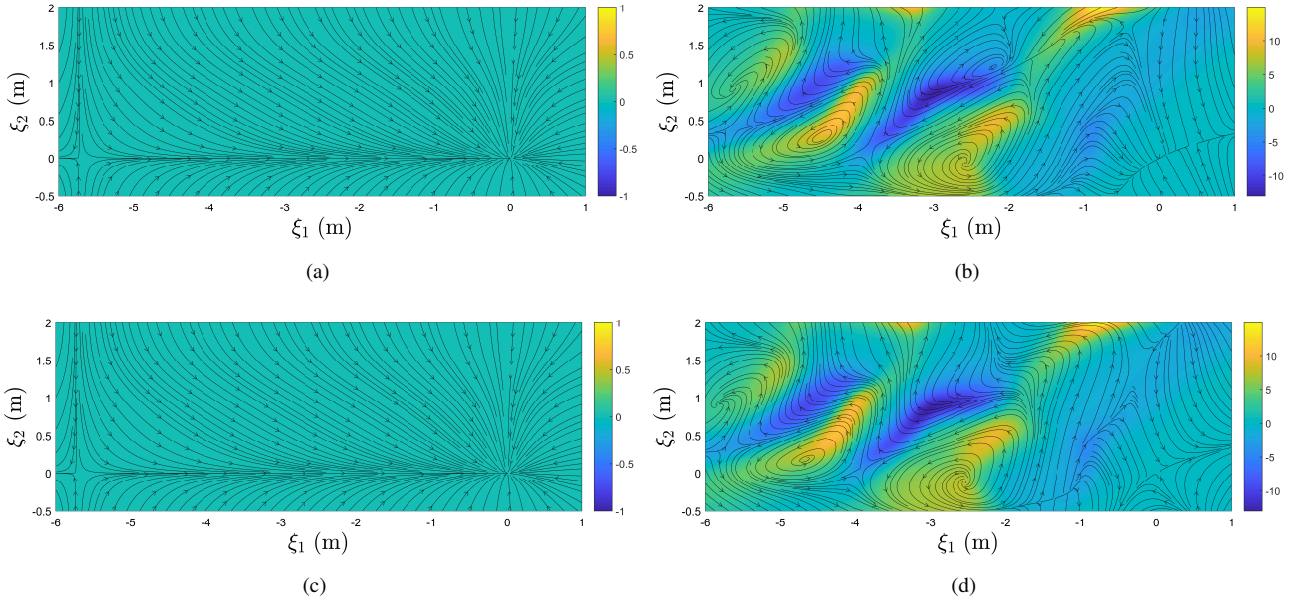


Figure 16. Schematic of DS decomposition in Section 6.3. The color of each point in the figure indicates the value of the angular velocity of the vector field at the corresponding point. Different decomposition methods and parameters correspond to different decomposition results: conservative DS (a) and non-conservative DS (b) correspond to $\omega = [1, 0]$, and conservative DS (c) and non-conservative DS (d) correspond to $\omega = [1, 1]$. (a) The conservative DS correspond to $\omega = [1, 0]$. (b) The non-conservative DS correspond to $\omega = [1, 0]$. (c) The conservative DS correspond to $\omega = [1, 1]$. (d) The non-conservative DS correspond to $\omega = [1, 1]$.

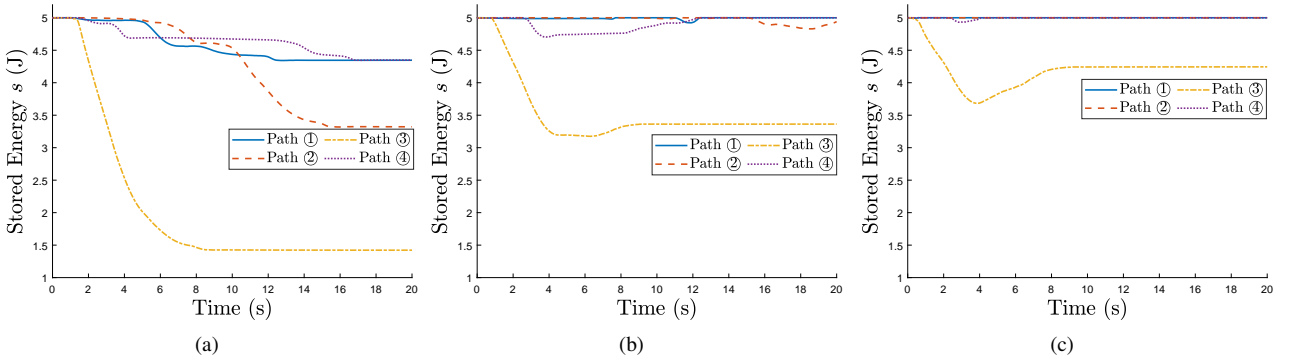


Figure 17. Schematic illustration of energy dissipation in the energy tank under different DS decomposition strategies. For each strategy, the robot moves along the representative four paths in Fig. 14(b). (a) The profile of the energy change corresponding to the DS in Fig. 14(a) without decomposition. (b) The profile of the energy change corresponding to the decomposition strategy $\omega = [1, 0]$. (c) The profile of the energy change corresponding to the decomposition strategy $\omega = [1, 1]$.

the conservative part is constant to zero. Unlike the 2D case, different decompositions correspond to non-conservative DSs with different angular velocity distributions, as shown in Figure 21(b) and Figure 21(d). This is due to the difference in the definition of the angular velocity of the 3D vector field from the 2D. Details can be found in Appendix D.

For a comprehensive comparison, we compare four controllers in simulation and experiment: 1) Using the nominal DS (61) without decomposition. 2) Using the nominal DS (61) and the decomposition strategy $\omega = [1, 0]$. 3) Using the nominal DS (61) and the decomposition strategy $\omega = [1, 1]$. 4) Using the projection DS in Section 6.4.1 as the nominal DS.

Figure 22 shows the change of the energy for four different strategies. The simulations and experiments show similar

trends. The energy decays the fastest when no decomposition is performed. After using the decomposition strategy $\omega = [1, 0]$, the energy decay is mitigated, but it still decays very fast. The enhancement obtained by using decomposition strategy $\omega = [1, 1]$ is limited. Unlike the case in Section 6.3, the decomposition strategy in this section has a limited effect on suppressing the energy decay. This is because the nominal DS (61), which represents the circular motion, is a curl field with a small conservative component in this section. Fortunately, the projection DS constructed in Section 6.4.1 can maintain the passivity without depleting the energy s (Proposition 2) and thus handles the special case well.

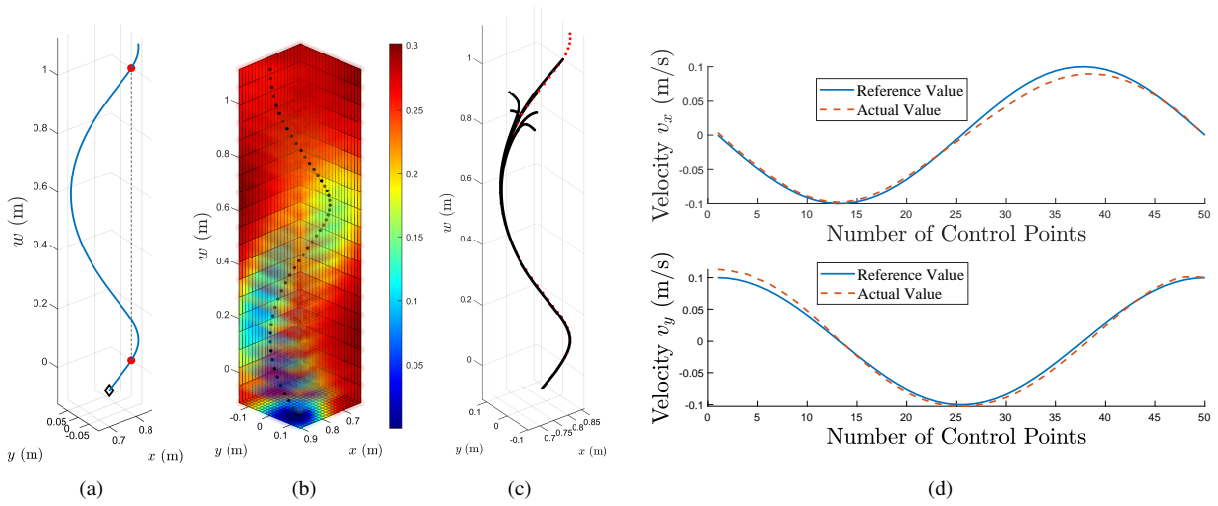


Figure 18. Schematic of the process of DS generation in high-dimensional space \mathbb{R}^{n+1} . w is the virtual coordinate. (a) Reference trajectory in high-dimensional space. (b) Potential energy function generated in high-dimensional space. The color indicates the value of the potential energy function. (c) DS generated in high-dimensional space. The black line represents the integral curve. (d) The velocity comparison. The actual velocity represents the result of learning through the GP.

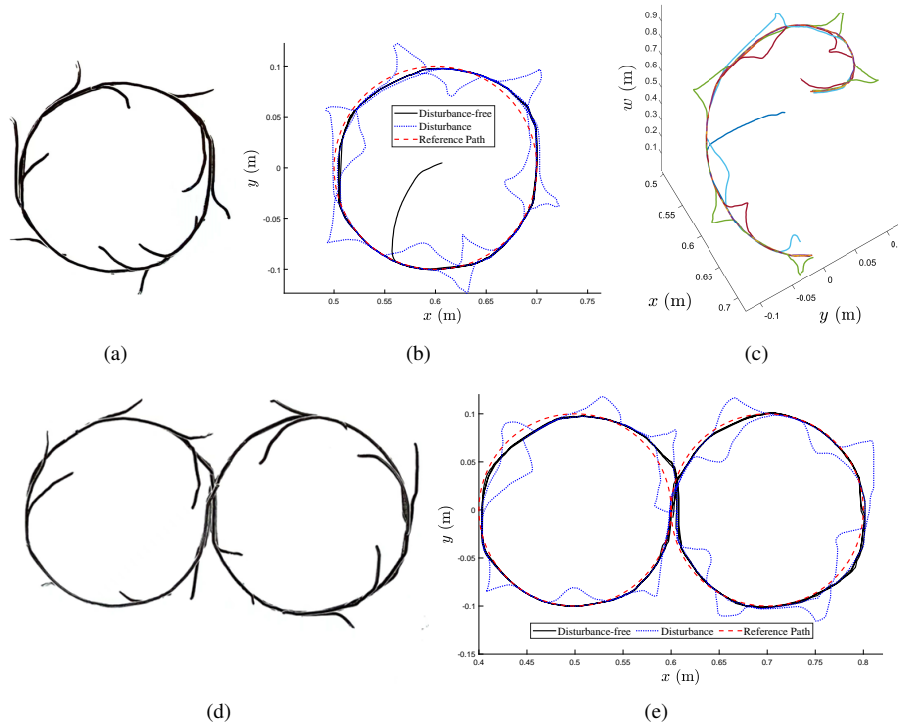


Figure 19. The experimental results for closed & self-intersecting motions on the plane. The result of the closed circle motion is shown in (a), (b) and (c). The results of the self-intersecting figure-of-eight movement are displayed in (d) and (e). (a) Trajectories of circular motion on the whiteboard under environmental disturbances. (b) Motion trajectories of circular motions under environmental disturbances. (c) Motion trajectories corresponding to circular motion in higher dimensional space \mathbb{R}^{n+1} under environmental disturbances. w is the virtual coordinate. (d) Trajectories of figure-of-eight movement on the whiteboard under environmental disturbances. (e) Motion trajectories of figure-of-eight movement under environmental disturbances.

7 Conclusion

7.1 Summary

In this paper, the stiffness encoding framework for modulating DS is presented. We give the quantitative effect of the combination between symmetry, exactness and

negative definiteness (contraction theory) of the stiffness matrix on the DS. For the problem of guaranteeing the passivity of the control system, we obtain the conservative DS based on the conservative stiffness matrix. We use GP to construct structure-specific potential energy functions so that the learned DS has symmetric attraction behavior, and

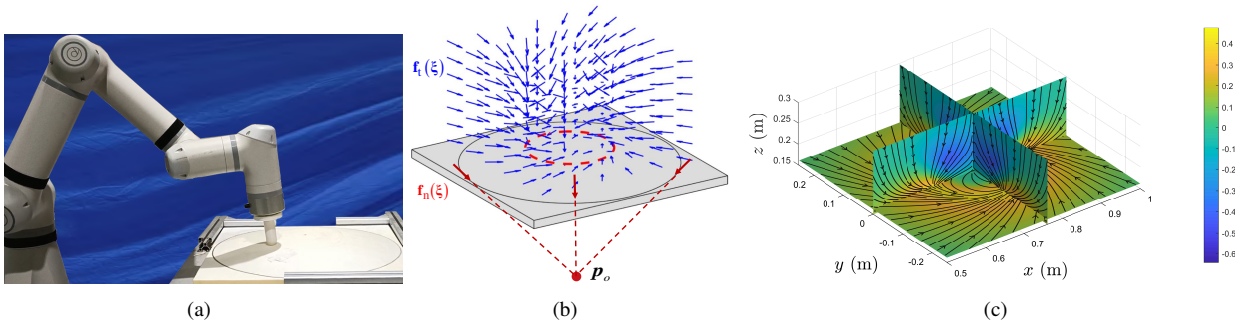


Figure 20. Schematic diagram of the experiment in Section 6.4.2. (a) Experimental setup. (b) The schematic of the original (pre-decomposition) DS in the experiment. $f_t(\xi)$ is the nominal DS, and $f_n(\xi)$ is the normal modulated DS. (c) The schematic of the original (pre-decomposition) DS $f_t(\xi)$ in Section 6.4.2. For clarity, we use three mutually perpendicular slices to show the 3D vector field and its angular velocity distribution. The color of each point in the figure indicates the value of the angular velocity of the vector field at the corresponding point.

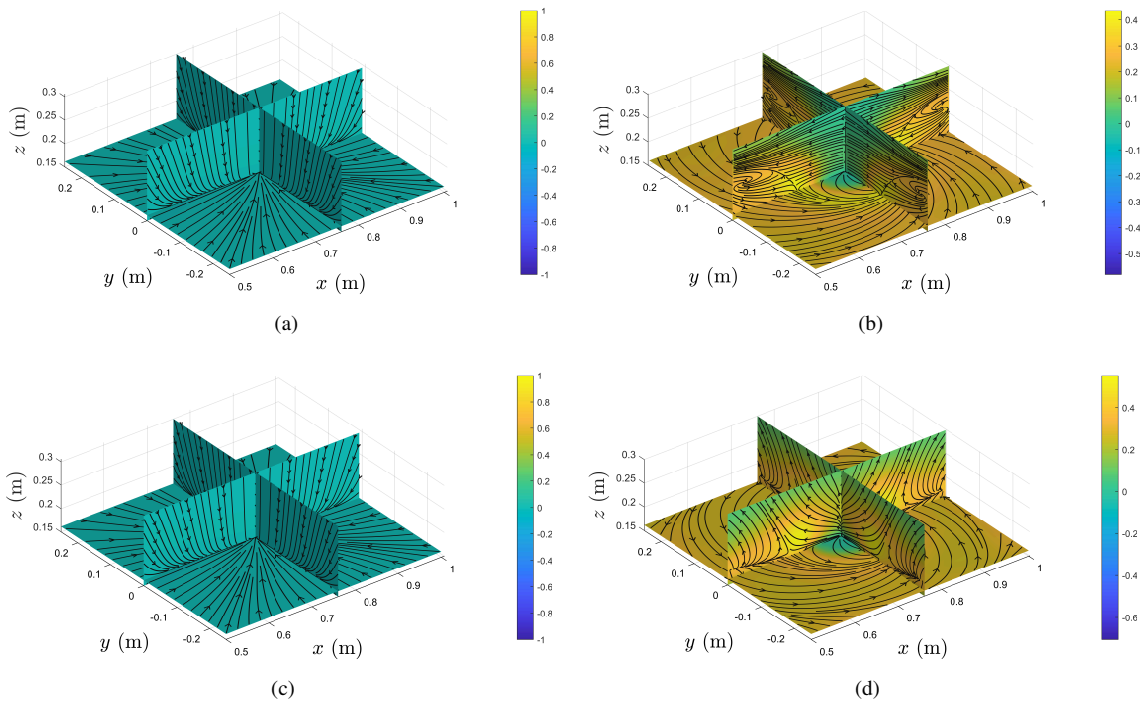


Figure 21. Schematic of DS decomposition in Section 6.4.2. For clarity, we use three mutually perpendicular slices to show the 3D vector field and its angular velocity distribution. The color of each point in the figure indicates the value of the angular velocity of the vector field at the corresponding point. Different decomposition methods and parameters correspond to different decomposition results: conservative DS (a) and non-conservative DS (b) correspond to $\omega = [1, 0]$, and conservative DS (c) and non-conservative DS (d) correspond to $\omega = [1, 1]$. (a) The conservative DS correspond to $\omega = [1, 0]$. (b) The non-conservative DS correspond to $\omega = [1, 0]$. (c) The conservative DS correspond to $\omega = [1, 1]$. (d) The non-conservative DS correspond to $\omega = [1, 1]$.

thus, the robotic system has better perturbation resistance. We further extend the conservative DS generation method to SE(3) and to special demonstration trajectories (e.g., closed and self-intersecting trajectories). We design the corresponding impedance control laws for the closed and self-intersecting trajectories to achieve the passivity of the control system without relying on the energy tank. For non-conservative DS, we construct a decomposition index considering the energy tank's structure. By optimizing the index, we decompose the vector field using a conservative stiffness matrix, which effectively slows down the energy

decay in the energy tank and improves the stability margin of the system.

We fully validate the theory and methodology of this paper through a series of simulations and experiments. Thanks to the DS's symmetric attraction behavior, the robot shows significant resistance to environmental perturbations when performing point-to-point motion tasks as well as closed and self-intersecting motion tasks. Meanwhile, the system's passivity in various motion scenarios is achieved by carefully designing the DS and the control law, and the robot exhibits advantageous robustness properties in the motion and human-robot interaction experiments.

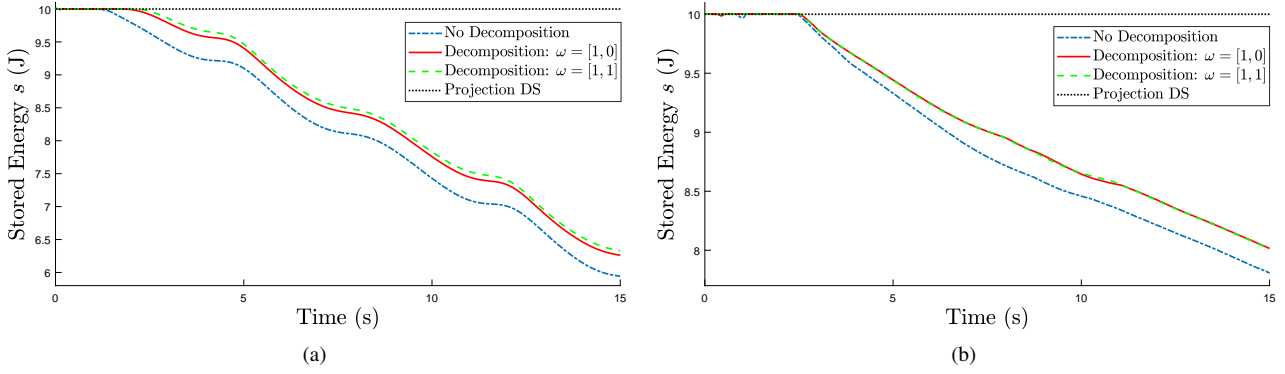


Figure 22. Schematic illustration of energy dissipation in the energy tank under different strategies. The blue dash-dot line indicates the case where the DS does not decompose. The red solid line corresponds to the decomposition strategy $\omega = [1, 0]$. The green dashed line corresponds to the decomposition strategy $\omega = [1, 1]$. The black dotted line corresponds to the high-dimensional projection DS. (a) The profile of the energy change in simulation. (b) The profile of the energy change in the experiment.

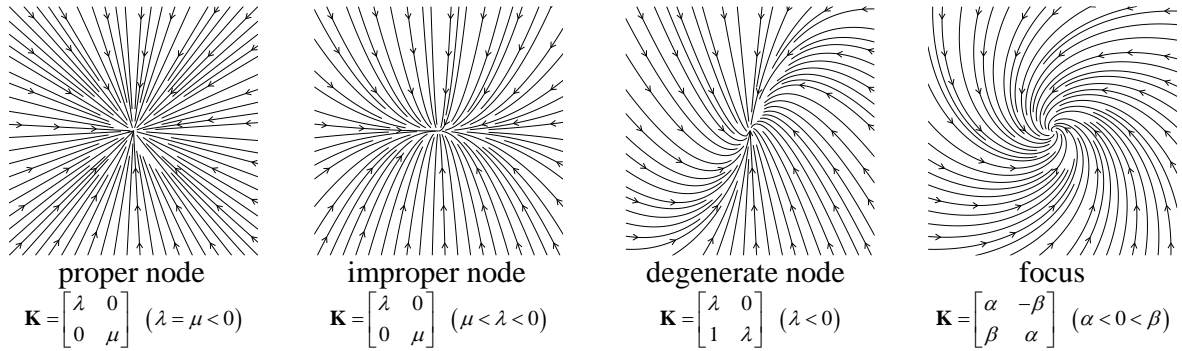


Figure 23. Schematic diagram of the local stiffness encoding. A rational construction can enable a nonlinear system $\dot{\xi} = f(\xi)$ to exhibit the same qualitative structure as a linear system $\dot{\xi} = \mathbf{K}\xi$ in the local domain of the equilibrium point ξ_0 . Different eigenvalue cases of the stiffness matrix \mathbf{K} correspond to different patterns: proper node, improper node, degenerate node and focus are illustrated in the figure.

7.2 Limitations and future developments

In this study, the controller could control the system in real time when the robot executes the motion. Since the GP involves the computation of the inverse of the matrix, when the spatial dimension of the motion continues to increase and the number of training points of the GP increases, the computation of the controller increases significantly, which may hinder the subsequent more comprehensive application. Moreover, the trajectories involved in this paper cover most of the robot's motion scenarios. However, when the complexity of the demonstration trajectories is further increased, the fitting accuracy will decrease, and the selection and optimization of some hyperparameters will become difficult. Using neural networks or other advanced methods may be an effective way to solve this problem. It is worth noting that other methods can still be naturally combined with the theory and methods in the subsequent sections of this paper after improving the method in Section 4.

The stiffness encoding framework proposed in Figure 1 focuses on analyzing the global properties (continuity, conservativeness, and contraction) of the DS. Based on stiffness encoding, we can also fine-tune the local properties of the DS, such as the system's qualitative structure in the local domain of the equilibrium point ξ_0 , as shown in

Figure 23. When a nonlinear system $\dot{\xi} = f(\xi)$ is dominated by a linear structure $\dot{\xi} = \mathbf{K}\xi$ near the equilibrium point, the qualitative structure of the system is determined by the linear part (Slotine and Li 1991).

Mohammadi et al. (2024) trained the neural network that generates the negative definite stiffness matrix and subsequently integrated the matrix to obtain the contractive DS. In this paper, our proposed stiffness encoding framework gives a series of important stiffness properties. Inspired by the above work, we can regulate the global and local properties of the DS by training the neural network to generate stiffness matrices of specific properties in the future.

Notice that the set of stiffness matrices with specific properties (symmetric, exact, negative definite, etc.) in this paper has the structure of a manifold or group. Generating the DS using matrices with specific properties can be considered an optimization process on matrix manifolds. Subsequent work can incorporate tools such as differential geometry to guide DS generation from an optimization perspective (Absil et al. 2008).

Acknowledgements

Tengyu Hou would like to thank Mr. Pingyun Nie, Mr. Sen Xu, Mr. Yuhang Chen and Mr. Jiexin Zhang for the valuable discussion.

Funding

The authors disclosed receipt of the following financial support for the research, authorship, and/or publication of this article: This work was partially supported by the National Natural Science Foundation of China (Grant Nos.51822506, 51935010).

References

- Absil PA, Mahony R and Sepulchre R (2008) *Optimization algorithms on matrix manifolds*. Princeton University Press.
- Albu-Schäffer A, Ott C and Hirzinger G (2007) A Unified Passivity-based Control Framework for Position, Torque and Impedance Control of Flexible Joint Robots. *The International Journal of Robotics Research* 26(1): 23–39.
- Amanhoud W, Hernandez Sanchez J, Bouri M and Billard A (2021) Contact-initiated shared control strategies for four-arm supernumerary manipulation with foot interfaces. *The International Journal of Robotics Research* 40(8-9): 986–1014.
- Amanhoud W, Khoramshahi M and Billard A (2019) A Dynamical System Approach to Motion and Force Generation in Contact Tasks. In: *Robotics: Science and Systems XV*. Robotics: Science and Systems Foundation.
- Amanhoud W, Khoramshahi M, Bonnesoeur M and Billard A (2020) Force Adaptation in Contact Tasks with Dynamical Systems. In: *2020 IEEE International Conference on Robotics and Automation (ICRA)*. Paris, France: IEEE, pp. 6841–6847.
- Blocher C, Saveriano M and Lee D (2017) Learning stable dynamical systems using contraction theory. In: *2017 14th International Conference on Ubiquitous Robots and Ambient Intelligence (URAI)*. Jeju: IEEE, pp. 124–129.
- Chen SF and Kao I (2000) Conservative congruence transformation for joint and cartesian stiffness matrices of robotic hands and fingers. *The International Journal of Robotics Research* 19(9): 835–847.
- Colgate JE and Hogan N (1988) Robust control of dynamically interacting systems. *International journal of Control* 48(1): 65–88.
- Dawson C, Gao S and Fan C (2023) Safe Control With Learned Certificates: A Survey of Neural Lyapunov, Barrier, and Contraction Methods for Robotics and Control. *IEEE Transactions on Robotics* 39(3): 1749–1767.
- Duan A, Batzianoulis I, Camoriano R, Rosasco L, Pucci D and Billard A (2024) A structured prediction approach for robot imitation learning. *The International Journal of Robotics Research* 43(2): 113–133.
- Duindam V, Stramigioli S and Scherpen J (2004) Passive Compensation of Nonlinear Robot Dynamics. *IEEE Transactions on Robotics and Automation* 20(3): 480–487.
- Ferraguti F, Secchi C and Fantuzzi C (2013) A tank-based approach to impedance control with variable stiffness. In: *2013 IEEE International Conference on Robotics and Automation*. Karlsruhe, Germany: IEEE, pp. 4948–4953.
- Fichera B and Billard A (2023) Hybrid Quadratic Programming - Pullback Bundle Dynamical Systems Control. In: *Robotics Research*, volume 27. Cham: Springer Nature Switzerland, pp. 387–394.
- Figueroa N and Billard A (2018) A Physically-Consistent Bayesian Non-Parametric Mixture Model for Dynamical System Learning. In: *Conference on Robot Learning (CoRL)*. pp. 927–946.
- Figueroa N and Billard A (2022) Locally active globally stable dynamical systems: Theory, learning, and experiments. *The International Journal of Robotics Research* 41(3): 312–347.
- Hogan N (1985) Impedance Control: An Approach to Manipulation: Part II—Implementation. *Journal of Dynamic Systems, Measurement, and Control* 107(1): 8–16.
- Hou T, Ding Y and Zhu X (2024) A geometric framework for stiffness mappings of compliant robotic systems on the special euclidean group. *IEEE Transactions on Robotics* 40: 2181–2200. DOI:10.1109/TRO.2023.3323824.
- Huber L, Trinca T, Slotine JJ and Billard A (2024) Passive Obstacle-Aware Control to Follow Desired Velocities. *IEEE Robotics and Automation Letters* : 1–8.
- Keppeler M, Lakatos D, Ott C and Albu-Schaffer A (2018) Elastic Structure Preserving (ESP) Control for Compliantly Actuated Robots. *IEEE Transactions on Robotics* 34(2): 317–335.
- Khadivar F and Billard A (2023) Adaptive Fingers Coordination for Robust Grasp and In-Hand Manipulation Under Disturbances and Unknown Dynamics. *IEEE Transactions on Robotics* 39(5): 3350–3367.
- Khansari-Zadeh SM and Billard A (2011) Learning stable nonlinear dynamical systems with gaussian mixture models. *IEEE Transactions on Robotics* 27(5): 943–957. DOI:10.1109/TRO.2011.2159412.
- Khansari-Zadeh SM and Khatib O (2017) Learning potential functions from human demonstrations with encapsulated dynamic and compliant behaviors. *Autonomous Robots* 41(1): 45–69.
- Kim S, Shukla A and Billard A (2014) Catching Objects in Flight. *IEEE Transactions on Robotics* 30(5): 1049–1065.
- Kishi Y, Zhi Wei Luo, Asano F and Hosoe S (2003) Passive impedance control with time-varying impedance center. In: *Proceedings 2003 IEEE International Symposium on Computational Intelligence in Robotics and Automation. Computational Intelligence in Robotics and Automation for the New Millennium (Cat. No.03EX694)*, volume 3. Kobe, Japan: IEEE, pp. 1207–1212.
- Koptev M, Figueroa N and Billard A (2024) Reactive collision-free motion generation in joint space via dynamical systems and sampling-based MPC. *The International Journal of Robotics Research* : 02783649241246557.
- Kronander K and Billard A (2016a) Passive interaction control with dynamical systems. *IEEE Robotics and Automation Letters* 1(1): 106–113. DOI:10.1109/LRA.2015.2509025.
- Kronander K and Billard A (2016b) Stability Considerations for Variable Impedance Control. *IEEE Transactions on Robotics* 32(5): 1298–1305.
- Kronander K, Khansari M and Billard A (2015) Incremental motion learning with locally modulated dynamical systems. *Robotics and Autonomous Systems* 70: 52–62.
- Lemme A, Neumann K, Reinhart R and Steil J (2014) Neural learning of vector fields for encoding stable dynamical systems. *Neurocomputing* 141: 3–14. DOI:https://doi.org/10.1016/j.neucom.2014.02.012.
- Li P and Horowitz R (1999) Passive velocity field control of mechanical manipulators. *IEEE Transactions on Robotics and Automation* 15(4): 751–763.
- Lohmiller W and Slotine JJE (1998) On Contraction Analysis for Non-linear Systems. *Automatica* 34(6): 683–696.

- Michel Y, Saveriano M and Lee D (2024) A Passivity-Based Approach for Variable Stiffness Control With Dynamical Systems. *IEEE Transactions on Automation Science and Engineering* : 1–12.
- Mohammad Khansari-Zadeh S and Billard A (2014) Learning control Lyapunov function to ensure stability of dynamical system-based robot reaching motions. *Robotics and Autonomous Systems* 62(6): 752–765.
- Mohammadi HB, Hauberg S, Arvanitidis G, Figueroa N, Neumann G and Rozo L (2024) Neural contractive dynamical systems. In: *The Twelfth International Conference on Learning Representations*.
- Neumann K and Steil JJ (2015) Learning robot motions with stable dynamical systems under diffeomorphic transformations. *Robotics and Autonomous Systems* 70: 1–15.
- Ott C (2008) *Cartesian impedance control of redundant and flexible-joint robots*. Springer.
- Ott C, Albu-Schaffer A, Kugi A and Hirzinger G (2008) On the Passivity-Based Impedance Control of Flexible Joint Robots. *IEEE Transactions on Robotics* 24(2): 416–429.
- Pérez-Dattari R and Kober J (2023) Stable Motion Primitives via Imitation and Contrastive Learning. *IEEE Transactions on Robotics* 39(5): 3909–3928.
- Perrin N and Schlehuber-Caissier P (2016) Fast diffeomorphic matching to learn globally asymptotically stable nonlinear dynamical systems. *Systems & Control Letters* 96: 51–59.
- Rana MA, Li A, Fox D, Boots B, Ramos F and Ratliff N (2020) Euclideanizing flows: Diffeomorphic reduction for learning stable dynamical systems. In: *Learning for Dynamics and Control*. PMLR, pp. 630–639.
- Ravichandar HC and Dani A (2019) Learning position and orientation dynamics from demonstrations via contraction analysis. *Autonomous Robots* 43(4): 897–912.
- Ravichandar HC, Salehi I and Dani AP (2017) Learning partially contracting dynamical systems from demonstrations. In: *CoRL*. pp. 369–378.
- Salehian SSM, Khoramshahi M and Billard A (2016) A Dynamical System Approach for Softly Catching a Flying Object: Theory and Experiment. *IEEE Transactions on Robotics* 32(2): 462–471.
- Slotine JJE and Li W (1991) *Applied nonlinear control*, volume 199. Prentice hall Englewood Cliffs, NJ.
- Spyrakos-Papastavridis E, Childs PRN and Dai JS (2020) Passivity Preservation for Variable Impedance Control of Compliant Robots. *IEEE/ASME Transactions on Mechatronics* 25(5): 2342–2353.
- Wang W and Slotine JJE (2005) On partial contraction analysis for coupled nonlinear oscillators. *Biological Cybernetics* 92(1): 38–53.
- Williams CK and Rasmussen CE (2006) *Gaussian processes for machine learning*, volume 2. MIT press Cambridge, MA.
- Yao W, de Marina HG, Lin B and Cao M (2021) Singularity-free guiding vector field for robot navigation. *IEEE Transactions on Robotics* 37(4): 1206–1221.

A DS Corresponding to the Conservative Stiffness

Next, we show the forms of the elastic force $\mathbf{f}(\boldsymbol{\xi})$ and potential function $V(\boldsymbol{\xi})$ corresponding to the conservative stiffness $\mathbf{K} = [k_{ij}]_{n \times n}$. We derive the following second-order partial differential equation from the symmetry and exactness of the conservative stiffness matrix:

$$\begin{cases} \frac{\partial k_{ki}}{\partial \xi^j} = \frac{\partial k_{kj}}{\partial \xi^i} \\ k_{ij} = k_{ji} \end{cases} \Rightarrow \begin{cases} \frac{\partial k_{ii}}{\partial \xi^j} = \frac{\partial k_{ij}}{\partial \xi^i} \\ \frac{\partial k_{jj}}{\partial \xi^i} = \frac{\partial k_{ji}}{\partial \xi^j} \end{cases} \Rightarrow \frac{\partial^2 k_{ii}}{\partial (\xi^j)^2} = \frac{\partial^2 k_{jj}}{\partial (\xi^i)^2}. \quad (62)$$

Then the generalized solution for the diagonal elements of \mathbf{K} can be expressed as $k_{ii}(\boldsymbol{\xi}) = \frac{\partial^2 g(\boldsymbol{\xi})}{\partial (\xi^i)^2}$, where $g(\boldsymbol{\xi})$ is an arbitrary differentiable function. The generalization of the non-diagonal elements of \mathbf{K} can be further obtained by substituting $k_{ii}(\boldsymbol{\xi})$ into (62):

$$\begin{cases} \frac{\partial k_{ii}}{\partial \xi^j} = \frac{\partial^3 g(\boldsymbol{\xi})}{\partial \xi^j \partial (\xi^i)^2} = \frac{\partial k_{ij}}{\partial \xi^i} \\ \frac{\partial k_{jj}}{\partial \xi^i} = \frac{\partial^3 g(\boldsymbol{\xi})}{\partial \xi^i \partial (\xi^j)^2} = \frac{\partial k_{ji}}{\partial \xi^j} \end{cases} \Rightarrow k_{ij} = k_{ji} = \frac{\partial^2 g(\boldsymbol{\xi})}{\partial \xi^i \partial \xi^j}. \quad (63)$$

In summary, the generalized solution of the stiffness matrix can be expressed as $\mathbf{K}(\boldsymbol{\xi}) = \left[\frac{\partial^2 g(\boldsymbol{\xi})}{\partial \xi^j \partial \xi^i} \right]_{n \times n}$.

The conservative elastic force $\mathbf{f}(\boldsymbol{\xi})$ can be obtained by integrating conservative stiffness matrix $\mathbf{K}(\boldsymbol{\xi})$:

$$\begin{aligned} \mathbf{f} &= \int_{\boldsymbol{\xi}_0}^{\boldsymbol{\xi}} \left[\frac{\partial^2 g(\boldsymbol{\xi})}{\partial \xi^j \partial \xi^i} \right]_{n \times n} \cdot d\boldsymbol{\xi} = \int_{\boldsymbol{\xi}_0}^{\boldsymbol{\xi}} d \left[\frac{\partial g(\boldsymbol{\xi})}{\partial \xi^i} \right]_{n \times 1} \quad (64) \\ &= \nabla g(\boldsymbol{\xi}) - \nabla g(\boldsymbol{\xi}_0). \end{aligned}$$

Integrating again yields an expression for the potential function $V(\boldsymbol{\xi})$:

$$\begin{aligned} V(\boldsymbol{\xi}) &= \int_{\boldsymbol{\xi}_0}^{\boldsymbol{\xi}} \mathbf{f} \cdot d\boldsymbol{\xi} = \int_{\boldsymbol{\xi}_0}^{\boldsymbol{\xi}} \nabla g(\boldsymbol{\xi}) \cdot d\boldsymbol{\xi} - \nabla g(\boldsymbol{\xi}_0) \cdot (\boldsymbol{\xi} - \boldsymbol{\xi}_0) \\ &= g(\boldsymbol{\xi}) - g(\boldsymbol{\xi}_0) - \nabla g(\boldsymbol{\xi}_0) \cdot (\boldsymbol{\xi} - \boldsymbol{\xi}_0). \quad (65) \end{aligned}$$

B Proof of Proposition 2

Proof. Next, we show that the system (1) controlled by (49) is passive with the storage function (50).

The change rate of the energy storage function (50) can be expressed as

$$\begin{aligned} \dot{W} &= \dot{\boldsymbol{\xi}}^T \mathbf{M}(\boldsymbol{\xi}) \ddot{\boldsymbol{\xi}} + \frac{1}{2} \dot{\boldsymbol{\xi}}^T \dot{\mathbf{M}}(\boldsymbol{\xi}) \dot{\boldsymbol{\xi}} \\ &\quad + \lambda_1 \nabla_{\boldsymbol{\xi}} V(\boldsymbol{\xi}, \boldsymbol{\xi}_{vir})^T \dot{\boldsymbol{\xi}} + \lambda_1 \frac{\partial V(\boldsymbol{\xi}, \boldsymbol{\xi}_{vir})}{\partial \boldsymbol{\xi}_{vir}} \dot{\boldsymbol{\xi}}_{vir} \\ &= \dot{\boldsymbol{\xi}}^T \left(\boldsymbol{\tau}_c + \boldsymbol{\tau}_e - \mathbf{C}(\boldsymbol{\xi}, \dot{\boldsymbol{\xi}}) \dot{\boldsymbol{\xi}} - \mathbf{g}(\boldsymbol{\xi}) \right) + \frac{1}{2} \dot{\boldsymbol{\xi}}^T \dot{\mathbf{M}}(\boldsymbol{\xi}) \dot{\boldsymbol{\xi}} \\ &\quad + \lambda_1 \nabla_{\boldsymbol{\xi}} V(\boldsymbol{\xi}, \boldsymbol{\xi}_{vir})^T \dot{\boldsymbol{\xi}} + \lambda_1 \frac{\partial V(\boldsymbol{\xi}, \boldsymbol{\xi}_{vir})}{\partial \boldsymbol{\xi}_{vir}} \dot{\boldsymbol{\xi}}_{vir} \\ &= \frac{1}{2} \dot{\boldsymbol{\xi}}^T (\dot{\mathbf{M}} - 2\mathbf{C}) \dot{\boldsymbol{\xi}} - \dot{\boldsymbol{\xi}}^T \mathbf{D}(\boldsymbol{\xi}, \boldsymbol{\xi}_{vir}) \dot{\boldsymbol{\xi}} + \dot{\boldsymbol{\xi}}^T \boldsymbol{\tau}_e \\ &\quad + \lambda_1 \dot{\boldsymbol{\xi}}^T \mathbf{f}_{pro}(\boldsymbol{\xi}, \boldsymbol{\xi}_{vir}) + \lambda_1 \nabla_{\boldsymbol{\xi}} V(\boldsymbol{\xi}, \boldsymbol{\xi}_{vir})^T \dot{\boldsymbol{\xi}} \\ &\quad + \lambda_1 \frac{\partial V(\boldsymbol{\xi}, \boldsymbol{\xi}_{vir})}{\partial \boldsymbol{\xi}_{vir}} \dot{\boldsymbol{\xi}}_{vir}. \quad (66) \end{aligned}$$

From the definition of the high-dimensional DS (46), we can obtain the following relation:

$$\begin{bmatrix} \dot{\boldsymbol{\xi}} \\ \dot{\xi}_{vir} \end{bmatrix} = \mathbf{f}(\boldsymbol{\xi}, \xi_{vir}) = - \begin{bmatrix} \nabla_{\boldsymbol{\xi}} V(\boldsymbol{\xi}, \xi_{vir}) \\ \frac{\partial V(\boldsymbol{\xi}, \xi_{vir})}{\partial \xi_{vir}} \end{bmatrix}, \quad (67a)$$

$$\mathbf{f}_{pro}(\boldsymbol{\xi}, \xi_{vir}) = \pi_{(1, \dots, n)}[\mathbf{f}(\boldsymbol{\xi}, \xi_{vir})] = -\nabla_{\boldsymbol{\xi}} V(\boldsymbol{\xi}, \xi_{vir}). \quad (67b)$$

Observe (67a), we have

$$\frac{\partial V(\boldsymbol{\xi}, \xi_{vir})}{\partial \xi_{vir}} \dot{\xi}_{vir} = - \left(\frac{\partial V(\boldsymbol{\xi}, \xi_{vir})}{\partial \xi_{vir}} \right)^2 \leq 0. \quad (68)$$

Notice that $(\dot{\mathbf{M}} - 2\mathbf{C})$ is a skew matrix while substituting (67b) and (68) into (66):

$$\dot{W} = -\dot{\boldsymbol{\xi}}^T \mathbf{D}(\boldsymbol{\xi}, \xi_{vir}) \dot{\boldsymbol{\xi}} + \lambda_1 \frac{\partial V(\boldsymbol{\xi}, \xi_{vir})}{\partial \xi_{vir}} \dot{\xi}_{vir} + \dot{\boldsymbol{\xi}}^T \boldsymbol{\tau}_e < \dot{\boldsymbol{\xi}}^T \boldsymbol{\tau}_e. \quad (69)$$

The inequality (69) means that the robotic system is passive under the controller (49).

C The Derivation of Conservative Fitting Function

Proof. We give details of the derivation of the fitting function $\hat{\mathbf{f}}_{\nu}(\boldsymbol{\xi})$ used in this paper.

For the three-dimensional linear space (i.e., $\boldsymbol{\xi} = [\xi_1 \ \xi_2 \ \xi_3]^T \in \mathbb{R}^3$), the simplest form of the conservative stiffness matrix is the diagonal matrix $\mathbf{K}(\boldsymbol{\xi}) = \text{diag}([\ k_{11}(\xi_1) \ k_{22}(\xi_2) \ k_{33}(\xi_3)]^T)$, which is simultaneously symmetric and exact. We choose cubic polynomials for parameterization:

$$\mathbf{K}_{\nu}(\boldsymbol{\xi}) = \text{diag} \left(\begin{bmatrix} \nu_1(\xi_1)^3 + \nu_2(\xi_1)^2 + \nu_3\xi_1 + \nu_4 \\ \nu_5(\xi_2)^3 + \nu_6(\xi_2)^2 + \nu_7\xi_2 + \nu_8 \\ \nu_9(\xi_3)^3 + \nu_{10}(\xi_3)^2 + \nu_{11}\xi_3 + \nu_{12} \end{bmatrix} \right), \quad (70)$$

where $\boldsymbol{\nu}$ is the parameter vector.

The conservative fitting function $\hat{\mathbf{f}}_{\nu}(\boldsymbol{\xi})$ can be obtained by integrating the conservative stiffness $\mathbf{K}_{\nu}(\boldsymbol{\xi})$:

$$\hat{\mathbf{f}}_{\nu}(\boldsymbol{\xi}) = \int_{\boldsymbol{\xi}_0}^{\boldsymbol{\xi}} \mathbf{K}_{\nu} d\boldsymbol{\xi} = \mathbf{f}_{\nu}(\boldsymbol{\xi}) - \mathbf{f}_{\nu}(\boldsymbol{\xi}_0), \quad (71)$$

where

$$\mathbf{f}_{\nu}(\boldsymbol{\xi}) = \begin{bmatrix} \nu_1(\xi_1)^4/4 + \nu_2(\xi_1)^3/3 + \nu_3(\xi_1)^2/2 + \nu_4\xi_1 \\ \nu_5(\xi_2)^4/4 + \nu_6(\xi_2)^3/3 + \nu_7(\xi_2)^2/2 + \nu_8\xi_2 \\ \nu_9(\xi_3)^4/4 + \nu_{10}(\xi_3)^3/3 + \nu_{11}(\xi_3)^2/2 + \nu_{12}\xi_3 \end{bmatrix}. \quad (72)$$

For the two-dimensional linear space (i.e., $\boldsymbol{\xi} = [\xi_1 \ \xi_2]^T \in \mathbb{R}^2$), $\mathbf{f}_{\nu}(\boldsymbol{\xi})$ can be expressed as

$$\mathbf{f}_{\nu}(\boldsymbol{\xi}) = \begin{bmatrix} \nu_1(\xi_1)^4/4 + \nu_2(\xi_1)^3/3 + \nu_3(\xi_1)^2/2 + \nu_4\xi_1 \\ \nu_5(\xi_2)^4/4 + \nu_6(\xi_2)^3/3 + \nu_7(\xi_2)^2/2 + \nu_8\xi_2 \end{bmatrix}. \quad (73)$$

In this paper, the use of a diagonal stiffness matrix in the simplest form and cubic polynomials produce good decomposition. For more complex cases, the non-diagonal stiffness matrix and higher-order polynomials can be further considered.

D Detailed Description of Angular Velocity

Proof. Next, we introduce the definition of the angular velocity Ω of the 2D and 3D vector fields, and further come to illustrate the effect of the vector field decomposition on the angular velocity Ω of the vector field.

1. The define of angular velocity Ω for the vector fields.

- (a) The 3D vector field:

The vector field can be expressed in the form of components:

$$\mathbf{f}(\boldsymbol{\xi}) = f_1(\boldsymbol{\xi})\mathbf{e}_1 + f_2(\boldsymbol{\xi})\mathbf{e}_2 + f_3(\boldsymbol{\xi})\mathbf{e}_3, \quad (74)$$

where \mathbf{e}_i is the coordinate base corresponding to ξ_i .

Then the curl of the vector field $\mathbf{f}(\boldsymbol{\xi})$ can be expressed as

$$\begin{aligned} \text{curl } \mathbf{f}(\boldsymbol{\xi}) &= \nabla \times \mathbf{f}(\boldsymbol{\xi}) = \left(\frac{\partial f_3}{\partial \xi_2} - \frac{\partial f_2}{\partial \xi_3} \right) \mathbf{e}_1 \\ &+ \left(\frac{\partial f_1}{\partial \xi_3} - \frac{\partial f_3}{\partial \xi_1} \right) \mathbf{e}_2 + \left(\frac{\partial f_2}{\partial \xi_1} - \frac{\partial f_1}{\partial \xi_2} \right) \mathbf{e}_3. \end{aligned} \quad (75)$$

The angular velocity of a 3D vector field is defined as the following scalar quantity:

$$\Omega = \frac{1}{2} (\nabla \times \mathbf{f}(\boldsymbol{\xi})) \cdot \frac{\mathbf{f}}{\|\mathbf{f}\|}. \quad (76)$$

- (b) The 2D vector field:

The vector field can be expressed in the form of components:

$$\mathbf{f}(\boldsymbol{\xi}) = f_1(\boldsymbol{\xi})\mathbf{e}_1 + f_2(\boldsymbol{\xi})\mathbf{e}_2. \quad (77)$$

Then the curl of the 2D vector field $\mathbf{f}(\boldsymbol{\xi})$ can be expressed as

$$\text{curl } \mathbf{f}(\boldsymbol{\xi}) = \nabla \times \mathbf{f}(\boldsymbol{\xi}) = \left(\frac{\partial f_2}{\partial \xi_1} - \frac{\partial f_1}{\partial \xi_2} \right) \mathbf{e}_3. \quad (78)$$

The angular velocity of the vector field is half the curl:

$$\Omega = \frac{1}{2} \text{curl } \mathbf{f}(\boldsymbol{\xi}) = \frac{1}{2} \left(\frac{\partial f_2}{\partial \xi_1} - \frac{\partial f_1}{\partial \xi_2} \right) \mathbf{e}_3. \quad (79)$$

2. The effect of vector field decomposition on angular velocity.

The Vector field $\mathbf{f}(\boldsymbol{\xi})$ have infinitely many different decompositions (show decomposition 1 and decomposition 2 below):

$$\mathbf{f}(\boldsymbol{\xi}) = \mathbf{f}_{c1}(\boldsymbol{\xi}) + \mathbf{f}_{nc1}(\boldsymbol{\xi}) = \mathbf{f}_{c2}(\boldsymbol{\xi}) + \mathbf{f}_{nc2}(\boldsymbol{\xi}). \quad (80)$$

Notice that the curl of the conservative vector field is zero:

$$\text{curl}(\mathbf{f}_{c1}(\boldsymbol{\xi})) = \text{curl}(\mathbf{f}_{c2}(\boldsymbol{\xi})) = \mathbf{0}. \quad (81)$$

Combining equations (80) and (81), we have

$$\text{curl}(\mathbf{f}(\boldsymbol{\xi})) = \text{curl}(\mathbf{f}_{nc1}(\boldsymbol{\xi})) = \text{curl}(\mathbf{f}_{nc2}(\boldsymbol{\xi})). \quad (82)$$

(82) shows that the original vector field $\mathbf{f}(\boldsymbol{\xi})$ has the same curl as the non-conservative component part $\mathbf{f}_{nc}(\boldsymbol{\xi})$ after decomposition.

(a) The 2D vector field:

Combining equations (82) and $\Omega = \frac{1}{2} \operatorname{curl} \mathbf{f}$, we have

$$\Omega(\mathbf{f}(\boldsymbol{\xi})) = \Omega(\mathbf{f}_{nc1}(\boldsymbol{\xi})) = \Omega(\mathbf{f}_{nc2}(\boldsymbol{\xi})). \quad (83)$$

(83) reveals the reason why Figure 15, 16(b), and 16(d) have the same pseudo-color.

(b) The 3D vector field:

Since angular velocity is defined as $\Omega = \frac{1}{2} \operatorname{curl} \mathbf{f} \cdot \frac{\mathbf{f}}{\|\mathbf{f}\|}$ and the directions of $\mathbf{f}_{nc1}(\boldsymbol{\xi})$ and $\mathbf{f}_{nc2}(\boldsymbol{\xi})$ are generally different, (83) no longer holds.